J. Fluid Mech. (2012), *vol.* 710, *pp.* 234–259.
doi:10.1017/jfm.2012.361

Influence of active control on STG-based generation of streamwise vortices in near-wall turbulence

B.-Q. Deng and C.-X. Xu†

Department of Engineering Mechanics, Tsinghua University, Beijing 100084, PR China

(Received 8 March 2011; revised 1 May 2012; accepted 13 July 2012;
first published online 29 August 2012)

Near-wall streamwise vortices are closely related to the generation of high skin friction in wall-bounded turbulent flows. A common feature of controlled, friction-reduced turbulent flows is weakened near-wall streamwise vortices. In the present study, the streak transient growth (STG) mechanism for generating near-wall streamwise vortices by Schoppa & Hussain (*J. Fluid Mech.*, vol. 453, 2002, pp. 57–108) is employed, and the opposition control proposed by Choi, Moin & Kim (*J. Fluid Mech.*, vol. 262, 1994, pp. 75–110) is imposed during the transient growth process of perturbations to determine how active control affects the generation of quasi-streamwise vortices. In the transient growth stage, when the detection plane is located near the wall ($y_d^+ = 15$), the control can suppress the production of streamwise vorticity by weakening the near-wall vertical velocity; when the detection plane moves away from the wall ($y_d^+ = 28$), the control has the opposite effect. In the vortex generation stage, the control cannot change the dominance of the stretching effect. Controls imposed at different stages reveal the importance of the STG stage in vortex generation. Strengthened out-of-phase control and lessened in-phase control are proposed as an extension of the original opposition-control scheme. Application in a fully developed turbulent channel flow shows that strengthened $y_d^+ = 10$ control can yield an even higher drag reduction rate than the original $y_d^+ = 15$ control. Moreover, lessened $y_d^+ = 28$ control can also achieve drag reduction and turbulence suppression.

Key words: drag reduction, turbulence control, turbulent boundary layers

1. Introduction

Near-wall quasi-streamwise vortices play a dominant role in both turbulence production and high skin-friction generation (Kim & Moin 1986; Kim, Moin & Moser 1987; Kravchenko, Choi & Moin 1993). Hence by active manipulation of these near-wall coherent structures, sustained turbulence suppression and friction-drag reduction may be achieved. Based on this scheme, Choi, Moin & Kim (1994) first proposed opposition control, which reduced the friction drag and alleviated near-wall streamwise vortices by applying instant blowing/suction velocity at the wall opposite to that detected at a small distance from the wall. Several more practical control schemes have been developed in accordance with this idea (Lee, Kim & Choi 1998; Endo, Kasagi & Suzuki 2000). The vast majority of subsequent works demonstrate that all

† Email address for correspondence: xucx@tsinghua.edu.cn

actively controlled friction-reduced flows share a common feature of weakened near-wall streamwise vortices; for recent reviews see Kim (2003), Collis *et al.* (2004), Kim & Bewley (2007), Kasagi, Suzuki & Fukagata (2009) and Kim (2011)). Nonetheless, how the quasi-streamwise vortices are suppressed is still ambiguous.

Several studies have tried to explain the mechanism for attenuating streamwise vortices by active opposition control. In addition to demonstrating the effectiveness of opposition control in drag reduction and turbulence suppression, Choi *et al.* (1994) also studied the influence of control on a two-dimensional vortex pair near the wall. They proposed that the control prevented the lifting process of the vortex pair and hence suppressed a source of new streamwise vortices above the wall. A similar explanation has also been proposed by Koumoutsakos (1997). However, these statements are based on a pair of two-dimensional vortices, thus ignoring the important three-dimensional effect on vortex generation in real turbulence. Furthermore, no attention was paid to the relation between control effect and detection location. Hammond, Bewley & Moin (1998) found that the optimal location of the detection plane, in terms of drag reduction rate, was around $y^+ = 15$. In this case, the maximum drag reduction rate of approximately 25 % was obtained and the near-wall streamwise vortices were greatly weakened. When the detection plane moves farther away from the wall ($y^+ = 25$), the friction drag drastically increased, together with the enhancement of streamwise vortices. Very recently, Chung & Talha (2011) studied the effects of strength and phase of wall blowing/suction in opposition control, and found that both amplitude and detection location play an important role in turbulence suppression and skin-friction reduction. By reducing the amplitude, opposition control with detection plane at $y^+ = 25$ could also achieve drag reduction and streamwise vortex attenuation. Hammond *et al.* (1998) and Chung & Talha (2011) both attributed the mechanism for drag reduction to the establishment of a 'virtual wall' between the real wall and the detection plane. The virtual wall concept can help us understand turbulence suppression and drag reduction from the viewpoint of hindering the vertical momentum transfer, but it can hardly explain the mechanism for streamwise vortex attenuation.

To draw a clearer picture of how active controls influence the evolution of near-wall streamwise vortices, a comprehensive understanding of the self-sustaining process of wall turbulence is necessary. In the near-wall region, low-speed streaks flanked by quasi-streamwise vortices are the predominant coherent structures. By ejecting low-speed fluid away from the wall and sweeping high-speed fluid towards the wall, the Reynolds shear stress is generated and turbulence is maintained. By gradually reducing the computational domain to the minimum value in the direct numerical simulation of turbulent Couette flow, Hamilton, Kim & Waleffe (1995) first observed a remarkably well-defined, quasi-cyclic, and spatially organized process of regeneration of these near-wall coherent structures. This process is composed of three distinct phases: the formation of streaks by streamwise vortices, the breakdown of streaks, and the regeneration of streamwise vortices. By artificially damping the fluctuations in the $y^+ > 60$ region, Jiménez & Pinelli (1999) further showed that the self-sustaining process in turbulent channel flow was autonomous in the sense that it was local to the near-wall region and did not depend on the outer flow. The existence of the near-wall self-sustaining process was also verified by the nonlinear travelling wave solution to the Navier–Stokes equations obtained in shear flows, which closely resembles the coherent structures observed in the near-wall region of turbulent flows (Nagata 1990; Waleffe 1998, 2001). Regarding the three stages in this self-sustaining process, the quasi-streamwise vortices acting on the mean shear are generally believed to create the

low-speed streaks (Waleffe 1997; Jiménez & Pinelli 1999; Panton 2001). However, no consensus has yet been reached on how the streamwise vortices are regenerated.

According to Panton (2001) and Schoppa & Hussain (2002), the explanations for the generation of streamwise vortices are categorized into two groups: the so-called parent–offspring mechanism (Bernard, Thomas & Handler 1993; Brooke & Hanratty 1993; Smith & Walker 1995; Zhou *et al.* 1999) and the instability-based mechanism (Swearingen & Blackwelder 1987; Robinson 1991; Hamilton *et al.* 1995; Waleffe 1997). In the parent–offspring mechanism, the new vortices are considered to be produced by the already existing vortices via the inflectional flow (Smith & Walker 1995), intense local shear layers (Zhou *et al.* 1999), and streamwise vorticity sheets (Bernard *et al.* 1993; Brooke & Hanratty 1993). The instability-based mechanism attributes the generation of streamwise vortices to the local instability of a quasi-steady base flow, without requiring the presence of parent vortices. The greatest concern is the streak instabilities (Robinson 1991; Hamilton *et al.* 1995) with the most dangerous perturbation of the sinuous streamwise mode (Waleffe 1997). Uniting the elements of the parent–offspring and instability-based scenarios, Schoppa & Hussain (2002) provided a more convincing mechanism, streak transient growth (STG), which was considered to be far more prevalent and energetic than the normal-mode instability. This STG-based scenario includes: (i) the transient growth of perturbations leading to the formation of a sheet of streamwise vorticity ω_x; (ii) growth of sinuous streak waviness and, hence, $\partial u/\partial x$ as the STG reaches a nonlinear amplitude; and (iii) the ω_x sheet's collapse via stretching by $\partial u/\partial x$ into streamwise vortices.

In the present study, this STG-based mechanism is employed to investigate how active opposition control interrupts the generation of streamwise vortices, and why the difference in detection location can have different – even opposite – effects on the flow, by performing direct numerical simulation of flows in a minimal channel (Jiménez & Moin 1991). The numerical method and STG problem formulation are first described in § 2, and the general response of the disturbance energy and vortical structure to control is introduced in § 3. The mechanism for control influencing the STG-based generation of streamwise vortices is analysed in § 4. Controls imposed at different stages are employed to validate the importance of the STG stage in § 5. Based on the knowledge obtained thus far, an extension to the original opposition-control scheme is proposed and tested in § 6. Finally, the summary and conclusion are given in § 7.

2. Problem formulation

The influence of active blowing/suction at the wall on STG-based generation of streamwise vortices is studied by performing direct numerical simulation of the incompressible flow of Newtonian fluid in a minimal channel. The Navier–Stokes equation written in rotational form

$$\frac{\partial \boldsymbol{V}}{\partial t} = \boldsymbol{V} \times \omega - \boldsymbol{\nabla} \Pi + \frac{1}{Re} \nabla^2 \boldsymbol{V}, \tag{2.1}$$

with the continuity constraint

$$\boldsymbol{\nabla} \cdot \boldsymbol{V} = 0, \tag{2.2}$$

is employed as the governing equation, in which $\boldsymbol{V}$ is the velocity vector, $\omega = \boldsymbol{\nabla} \times \boldsymbol{V}$ the vorticity vector, and $\Pi = p/\rho + |\boldsymbol{V}|^2/2$ the total pressure. The equations are non-dimensionalized by bulk mean velocity U_m and channel half-width H, and hence

the Reynolds number is defined as $Re = U_m H/\nu$, in which ν is the kinematic viscosity of the fluid. The streamwise, wall-normal, and spanwise coordinates are represented by x, y and z, respectively, and u, v, w are the corresponding velocity components.

In the streamwise and spanwise directions, the flow is assumed periodic over the lengths of $2\pi/\alpha$ and $2\pi/\beta$, respectively, in which α and β are the basic wavenumbers in the streamwise and spanwise directions. In the wall-normal direction y, a no-slip condition is imposed at the walls, $y = \pm 1$. In the case of control, active blowing and suction are enforced at the lower wall according to the opposition-control scheme, that is, the wall-normal velocity component at $y = -1$ is specified to be the opposite of the wall-normal velocity component detected at y_d,

$$v(x, -1, z, t) = -v(x, y_d, z, t). \tag{2.3}$$

In the present study, two detection positions have been tested: $y_d^+ = 15$, which is considered to be the optimal position in terms of the drag reduction rate, and $y_d^+ = 28$, which can cause a drastic increase in friction drag (Hammond *et al.* 1998; Chung & Talha 2011).

The governing equations (2.1) and (2.2) are solved by a pseudo-spectral method for spatial discretization. The Fourier–Galerkin method is used in the streamwise and spanwise directions, and the Chebyshev–tau method is adopted for the wall-normal direction. Dealiasing is applied in the x and z directions using the 3/2 rule. The third-order time-splitting method is employed for time advancement. The code has been validated through the direct comparison of turbulence statistics with the results from the literature (Kim *et al.* 1987), and has already been used in several applications concerning direct numerical simulation of turbulent channel flows; see Xu *et al.* (1996) and Cui *et al.* (2004) for related publications.

In the present study, the Reynolds number is chosen to be $Re = 2800$, corresponding to the friction Reynolds number around $Re_\tau = 180$. According to Jiménez & Moin (1991), the computational domain is selected to span $\pi \times 2 \times 0.2\pi$ (approximately $560 \times 360 \times 110$ wall units) in the streamwise, wall-normal, and spanwise directions, respectively, to obtain sustained turbulence and isolate only one low-speed streak in the domain. Accordingly, $32 \times 129 \times 32$ grids are used.

According to Schoppa & Hussain (2002), the flow field is initialized by the single-side turbulent profile with a low-speed streak as the base flow,

$$U(y, z) = U_0(y) + \tfrac{1}{2}\Delta u \cos(\beta z) g(y), \quad V = W = 0, \tag{2.4}$$

and the streamwise dependent spanwise velocity w' is used as the perturbation referred to as STG perturbation in Schoppa & Hussain (2002) and hereinafter:

$$u' = 0, \quad v' = 0, \quad w' = A \sin(\alpha x) g(y). \tag{2.5}$$

Here, the superscript $'$ denotes the perturbations to the two-dimensional base flow $U(y, z)$.

In (2.4), $U_0(y)$ is composed of a laminar profile near the upper wall and a turbulent profile near the lower wall, as was adopted by Schoppa & Hussain (2002):

$$U_0(y) = \begin{cases} U_c \left[1 - \left(\dfrac{y}{H} - 1\right)^2\right], & y_m \leqslant y \leqslant 2H, \\ u_\tau \left[2.5 \ln(1 + 0.4y^+) + 7.8(1 - \mathrm{e}^{-y^+/11}) - \dfrac{y^+}{11}\mathrm{e}^{-0.33y^+}\right], & 0 \leqslant y < y_m. \end{cases} \tag{2.6}$$

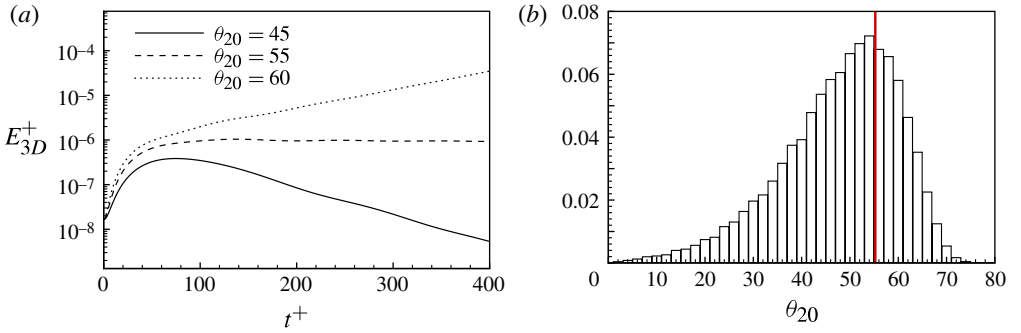

FIGURE 1. (*a*) Time evolution of disturbance energy upon streaks with $\theta_{20} = 45$, 55 and 60°; (*b*) histogram of streak lift angle θ_{20}, conditionally sampled from DNS data of fully developed turbulent channel flow at $Re_\tau = 180$. The bold line denotes the threshold θ_{20} for linear normal mode instability.

Notably, the Reynolds number in the present study is almost twice as high as that of Schoppa & Hussain (2002), while the parameters u_τ, y_m and U_c to determine the distribution of $U_0(y)$ are recalculated to match the present Reynolds number $Re_\tau = 180$. The profile on the turbulent side obtained according to (2.6) has been compared with that obtained in the full-scale channel at the same Reynolds number (Kim *et al.* 1987), and they show good agreement. The low-speed streak is represented by $\Delta u \cos(\beta z) g(y)$, in which the spanwise wavenumber β is chosen to make the streak span approximately 110 wall units in the spanwise direction, and $g(y)$ takes the form of $y\exp(-\eta y^2)$. We select η to make $g(y)$ reach the maximum value at $y^+ = 20$. Once $g(y)$ is fixed, Δu is determined by the streak strength. According to Schoppa & Hussain (2002), the streak strength is quantified by the vortex line lift angle at $y^+ = 20$ as $\theta_{20} = \tan^{-1}(|\Omega_y|_{max}/|\Omega_z|)_{y^+=20}$, with $\Omega_y = \partial U/\partial z$ and $\Omega_z = -\mathrm{d}U_0/\mathrm{d}y$. In the following, for the normal mode stability analysis, the frozen base flow is adopted to determine the threshold streak strength. Because active control applied to the fully developed turbulent channel flow can greatly change the mean value of wall skin friction, that is, $\mathrm{d}U_0/\mathrm{d}y$ at the wall, to mimic this effect in minimal channel flow, no body force is used to prevent the viscous diffusion of the initial profile $U_0(y)$ for STG analysis.

To choose the streak strength θ_{20}, the threshold streak strength for the linear normal-mode instability at the present Reynolds number should be determined first. The evolutions of the STG perturbation (2.5) with infinitesimal amplitude are studied by direct numerical simulation upon frozen streaks with different θ_{20}. Figure 1(*a*) shows the time evolution of disturbance energy $E_{3D} = (u'^2 + v'^2 + w'^2)/2$ upon streaks with $\theta_{20} = 45$, 55 and 60°. After transient growth, the disturbance energy for $\theta_{20} = 45°$ and $\theta_{20} = 60°$ experiences exponential decrease and increase, respectively, whereas that for $\theta_{20} = 55°$ remains constant, indicating that the streak with $\theta_{20} = 55°$ is neutrally stable. This value is slightly higher than that obtained by Schoppa & Hussain (2002) ($\theta_{20} \approx 50°$) at a relatively lower Re_τ. Using the same conditional streak sampling technique as that by Schoppa & Hussain (2002), the histogram of θ_{20} statistics in fully developed turbulent channel flow at $Re_\tau = 180$ is obtained, as shown in figure 1(*b*). Approximately 70 % of streaks are normal-mode stable. Although the ratio is a bit lower than the 80 % obtained by Schoppa & Hussain (2002) at $Re_\tau \approx 90$, this STG-based vortex generation scenario is still prevalent.

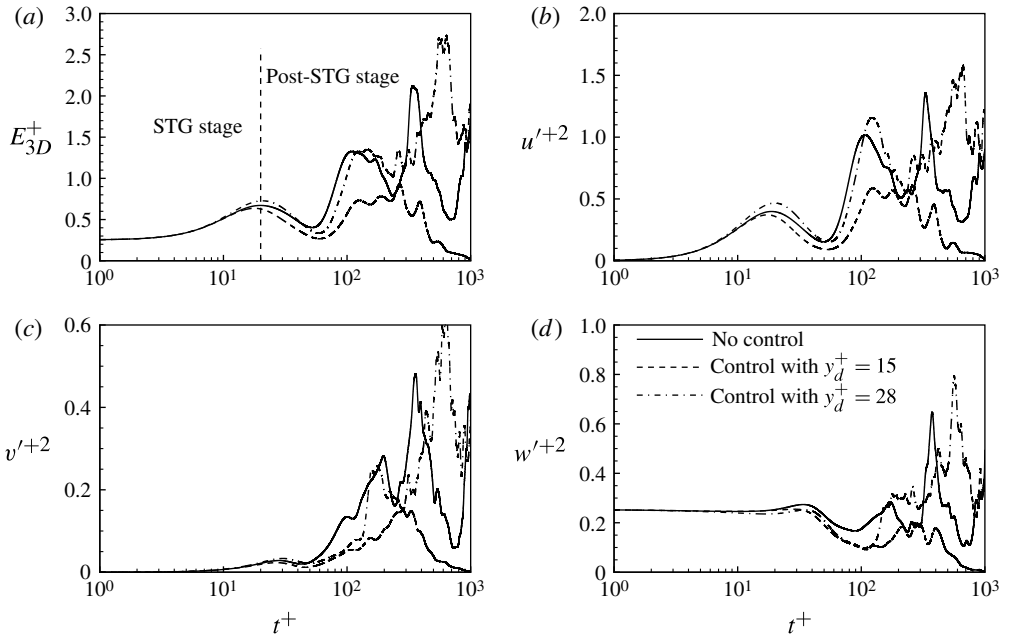

FIGURE 2. Time evolution of (*a*) E_{3D}, (*b*) u'^2, (*c*) v'^2, and (*d*) w'^2 in non-controlled and opposition-controlled minimal channel flows.

As addressed above, the more prominent STG-based vortex generation mechanism is considered in the present study. Hence, the normal-mode stable streak with $\theta_{20} = 45°$ and the initial STG perturbation at a magnitude of $w_{rms}^+ = 0.5$ are chosen for the detailed analysis presented in §§ 3 and 4. A streak with $\theta_{20} = 50°$ and $w_{rms}^+ = 0.3$ is also used to evaluate the influence of the initial conditions and to study the effect of control imposed at different stages in § 5.

3. Evolution of disturbance energy and vortical structure

The time evolutions of disturbance energy E_{3D} and its components u'^2, v'^2, and w'^2 in non-controlled and opposition-controlled minimal channel flows are shown in figure 2. For all the cases, E_{3D} undergoes transient growth before $t^+ = 20$, and fluctuates thenceforth. The periods of $t^+ < 20$ and $t^+ > 20$ are referred to as the STG and the post-STG stages, respectively, as shown in figure 2(*a*). In the STG stage, the transient growth of u' is the dominant mechanism. u' reaches a peak value at $t^+ = 20$, which is consistent with the time of maximum transient energy growth in work by del Álamo & Jiménez (2006) and Pujals *et al.* (2009). The amplification of v' is milder, and reaches a far lower peak value later at $t^+ = 30$. Unlike u' and v', w' is almost unchanged and keeps the initial amplitude until the end of the STG stage. The control with $y_d^+ = 15$ weakens the growth of E_{3D}, but that with $y_d^+ = 28$ strengthens it. At the end of the STG stage, E_{3D} reaches a different peak value of 0.67, 0.63 and 0.73 for the cases of no control, $y_d^+ = 15$ control and $y_d^+ = 28$ control, respectively. In the post-STG stage, the nonlinear effects play an important role and result in the generation of quasi-streamwise vortices, as indicated by Schoppa & Hussain (2002). They are also discussed in the next section. At this stage, the $y_d^+ = 15$ control suppresses all three components of E_{3D}, which are enhanced by the $y_d^+ = 28$ control.

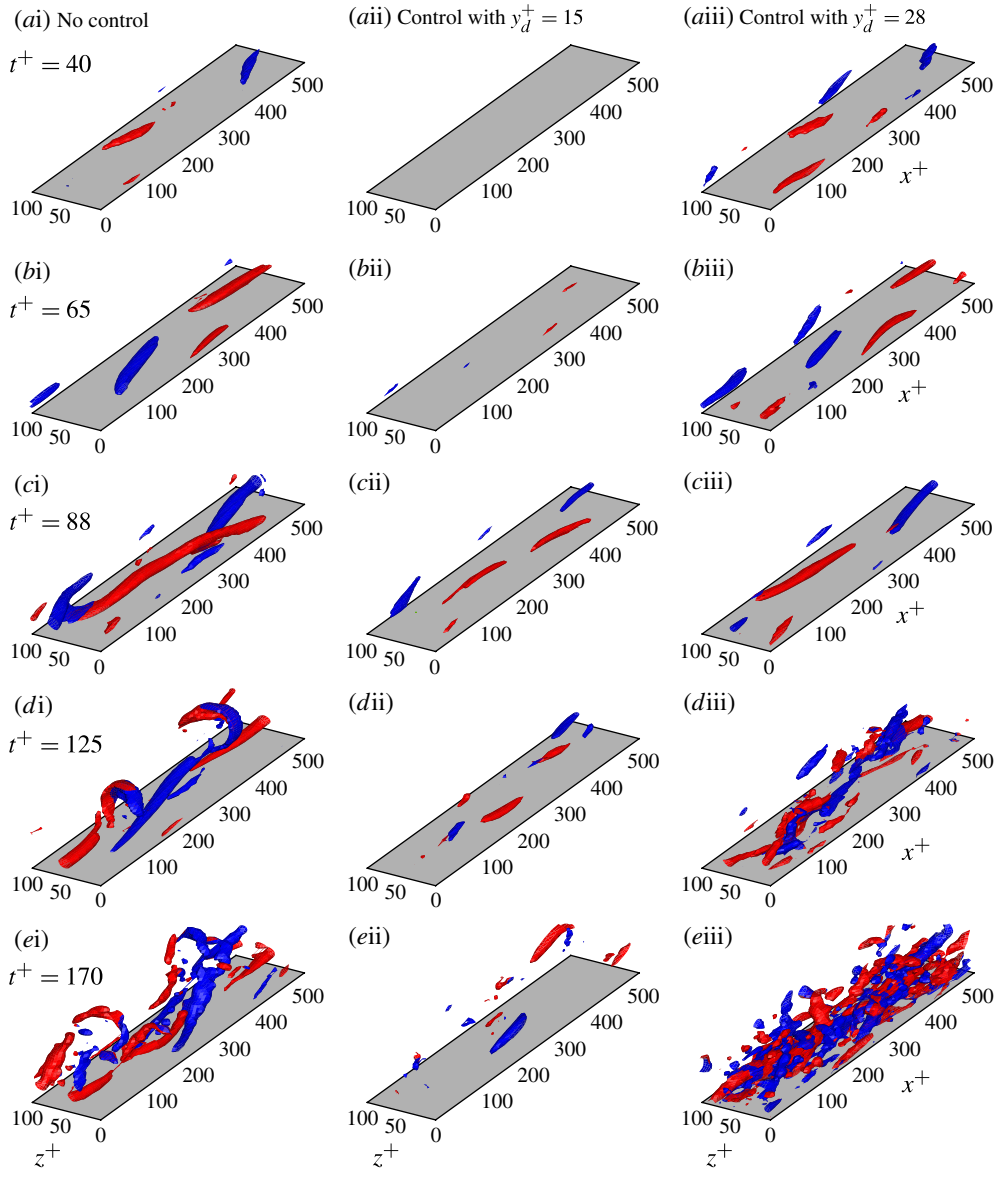

FIGURE 3. (Colour online) Iso-surface of $\lambda_2 = -3$ at (*a*i–*a*iii) $t^+ = 40$, (*b*i–*b*iii) $t^+ = 65$, (*c*i–*c*iii) $t^+ = 88$, (*d*i–*d*iii) $t^+ = 125$, and (*e*i–*e*iii) $t^+ = 170$ for (*a*i–*e*i) no control, (*a*ii–*e*ii) $y_d^+ = 15$ control, and (*a*iii–*e*iii) $y_d^+ = 28$ control. Red (light), $\omega_x > 0$; blue (dark), $\omega_x < 0$.

The vortical structures are identified and visualized by the iso-surface of $\lambda_2 < 0$ (Jeong & Hussain 1995). Figure 3 shows the iso-surface of $\lambda_2 = -3$ at $t^+ = 40$, 65, 88, 125 and 170 for the no-control and the two opposition-control cases, respectively, to display the generation and evolution process of vortices. Notably, due to blowing and suction at the wall, vortical structures that could be identified by negative λ_2 are generated adjacent to the wall. The vortical structures below $y^+ = 5$ are removed in figure 3 to clearly illustrate the effect of control on near-wall streamwise vortices. For the no-control case, quasi-streamwise vortices are formed at $t^+ = 40$, and gradually

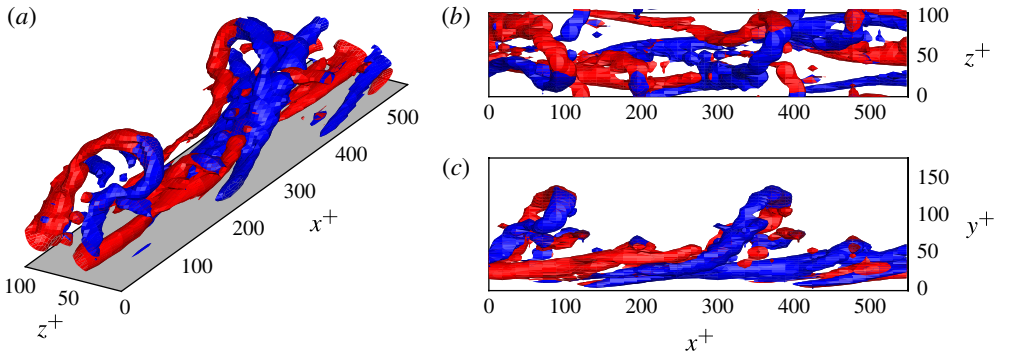

FIGURE 4. (Colour online) Iso-surface of $\lambda_2 = -1.5$ at $t^+ = 170$ for the no-control case: (*a*) overview, (*b*) top view, and (*c*) side view. Red (light), $\omega_x > 0$; blue (dark), $\omega_x < 0$.

elongated in the streamwise direction (figure 3*a*i–*c*i). At $t^+ = 125$, as shown by figure 3(*d*i), the elongated streamwise vortices are lifted up from the wall and a spanwise arc is produced from the lifted downstream end of the vortices, forming a hook or asymmetric hairpin vortex, as named by Robinson (1991). At $t^+ = 170$, the spanwise arcs are connected to the lifted quasi-streamwise vortices at another side, and the more symmetric hairpin vortices are formed (figure 3*e*i). The hairpin vortices are more clearly displayed in figure 4 by the iso-surface of $\lambda_2 = -1.5$. The side view shown in figure 4(*c*) indicates that the arc head is formed around $y^+ = 100$. In the work of Schoppa & Hussain (2002), the formation of the spanwise arc head was not reported. The reason may be that the maximum y^+ on the turbulence side is around 90 in their simulation; hence, there is not enough space for the development of the arc head. This is consistent with the finding of Jiménez & Simens (2001) that the formation of asymmetric hairpins by ejection was prevented by damping the disturbances above $y^+ = 70$ in a minimal turbulent channel flow. Compared with the no-control case, the streamwise vortices are greatly attenuated by the $y_d^+ = 15$ control from the very beginning of the vortex generation process until the turbulence stage (figure 3*a*ii–*e*ii). At $t^+ = 40$, the vortices are too weak to be displayed by $\lambda_2 = -3$ and therefore no structures are shown in figure 3(*a*ii). On the other hand, by the $y_d^+ = 28$ control for $t^+ < 125$, the streamwise vortices have a similar strength to the no-control case (figure 3*a*iii–*c*iii), but with shorter streamwise length. At $t^+ \geqslant 125$, the vortices are evidently increased in number compared with the no-control case.

The response of the disturbance energy and streamwise vortices to opposition control with different y_d^+ in minimal channel flow are consistent with those in the full-scale channel flow (Choi *et al.* 1994): the $y_d^+ = 15$ control could attenuate the near-wall streamwise vortices, reduce skin friction, and suppress turbulence intensity (see figures 19 and 20), whereas the $y_d^+ = 28$ control has the opposite effects. The underlying mechanism for this observed scenario is explained in the following section by analysing streamwise vorticity transport in the STG and post-STG stages, respectively.

4. Mechanism for control influencing the generation of streamwise vortices

4.1. *The STG stage*

According to Schoppa & Hussain (2002), no streamwise vortices could be generated in the STG stage, but the streamwise vorticity ω_x and the spanwise meandering of low-

speed streaks represented by $\partial u'/\partial x$ may be transiently amplified, which is necessary to trigger the nonlinear stretching effect to form streamwise vortices in the post-STG stage. The influence of control on the evolution and distribution of ω_x and $\partial u'/\partial x$ is discussed in the following. Because control is imposed through the vertical velocity at the wall, its effect on v' would be more straightforward and is analysed first. The changes in $\partial u'/\partial x$ and ω_x are then described subsequently.

The initial disturbance is of finite amplitude, and therefore the nonlinear equations for perturbations with the continuity constraint are considered to analyse the behaviour of the flow, as shown in the following:

$$\frac{\partial u'}{\partial t} = -U\frac{\partial u'}{\partial x} - v'\frac{\partial U}{\partial y} - w'\frac{\partial U}{\partial z} - \frac{\partial p'}{\partial x} - \left(u'\frac{\partial u'}{\partial x} + v'\frac{\partial u'}{\partial y} + w'\frac{\partial u'}{\partial z}\right), \tag{4.1}$$

$$\frac{\partial v'}{\partial t} = -U\frac{\partial v'}{\partial x} - \frac{\partial p'}{\partial y} - \left(u'\frac{\partial v'}{\partial x} + v'\frac{\partial v'}{\partial y} + w'\frac{\partial v'}{\partial z}\right), \tag{4.2}$$

$$\frac{\partial w'}{\partial t} = -U\frac{\partial w'}{\partial x} - \frac{\partial p'}{\partial z} - \left(u'\frac{\partial w'}{\partial x} + v'\frac{\partial w'}{\partial y} + w'\frac{\partial w'}{\partial z}\right), \tag{4.3}$$

$$\frac{\partial u'}{\partial x} + \frac{\partial v'}{\partial y} + \frac{\partial w'}{\partial z} = 0. \tag{4.4}$$

Notably, all the nonlinear terms are placed in the parentheses on the right-hand sides of the equations, and the viscous terms are omitted because they are not essential to the growth mechanism (Schoppa & Hussain 2002).

First, the distribution of v' in the wall-normal direction is analysed. Initially, $u' = v' = 0$, and we only have w' in the form of (2.5) upon the base flow $U(y, z)$. In the early STG stage, the leading-order terms on the right-hand side of (4.1)–(4.3) are the linear terms related to w' and U, that is, $-w'\partial U/\partial z$ and $-U\partial w'/\partial x$. The DNS results show that all the other terms are at least one order of magnitude smaller than these two terms at $t^+ = 1$. According to (4.1), the generation rate of u' is nearly proportional to $-w'\partial U/\partial z$. Hence, $\partial u'/\partial x$ varies as $-(\partial w'/\partial x)(\partial U/\partial z)$. Viewing $-w'\partial U/\partial z$ as an analogy to a body force in the streamwise direction, the distribution of u' is similar to the oblique perturbations that reach maximum energy growth under a streamwise direction force in the work of Jovanovic & Bamieh (2005). For w', the dominant term on the right-hand side of (4.3) is $-U\partial w'/\partial x$, and therefore $\partial w'/\partial z \sim -(\partial w'/\partial x)(\partial U/\partial z)$. Considering the continuity constraint, we could obtain the Poisson equation for p' as

$$\frac{\partial^2 p'}{\partial x^2} + \frac{\partial^2 p'}{\partial y^2} + \frac{\partial^2 p'}{\partial z^2} = -2\frac{\partial w'}{\partial x}\frac{\partial U}{\partial z}. \tag{4.5}$$

The above analysis shows that $\partial v'/\partial y \sim -(\partial u'/\partial x + \partial w'/\partial z) \sim 2(\partial w'/\partial x)(\partial U/\partial z)$. Considering the form of base flow and STG perturbation in (2.4) and (2.5), v' should vary with x and z as $\cos(\alpha x)$ and $\sin(\beta z)$, respectively. According to (4.2), $v' \sim -\partial p'/\partial y$, hence the pressure p' should take the form of $p' = \hat{p}(y)\cos(\alpha x)\sin(\beta z)$. Considering (2.4) and (2.5), we can get

$$\frac{\mathrm{d}^2\hat{p}}{\mathrm{d}y^2} - (\alpha^2 + \beta^2)\hat{p} = A\alpha\beta\Delta u g^2(y). \tag{4.6}$$

Equation (4.6) is solved by the Chebyshev–tau method subjected to the boundary condition of $\mathrm{d}\hat{p}/\mathrm{d}y = 0$ at the walls. Figure 5 shows the distribution of $\mathrm{d}\hat{p}/\mathrm{d}y$ normalized by its maximum value. The zero-crossing point of $\mathrm{d}\hat{p}/\mathrm{d}y$ is

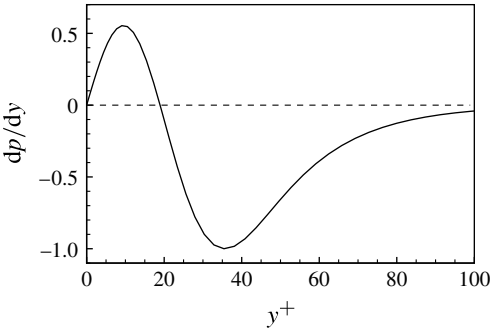

FIGURE 5. Distribution of $\mathrm{d}\hat{p}/\mathrm{d}y$ in the wall-normal direction.

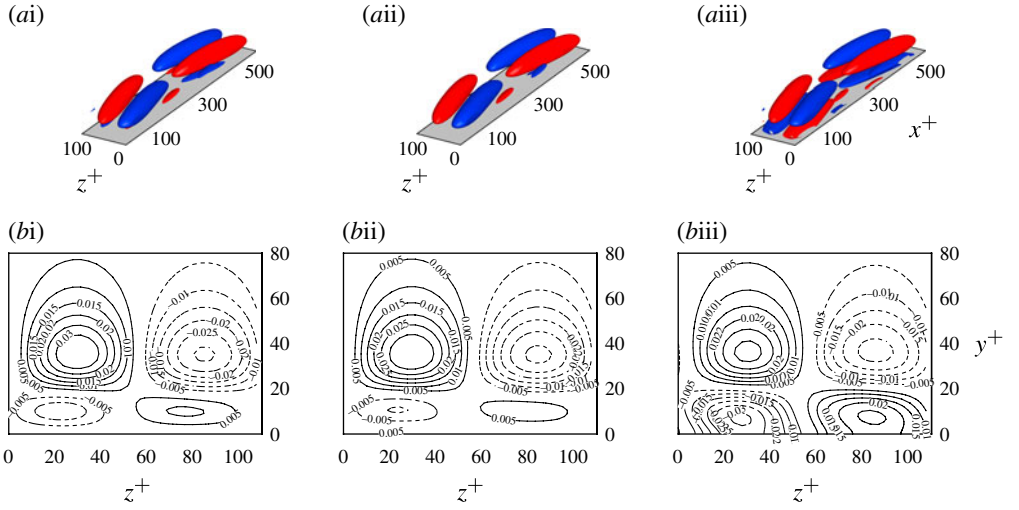

FIGURE 6. (Colour online) (*a*i–*a*iii) Iso-surface of $|v'| = 0.01$ and (*b*i–*b*iii) contours of v' on the (y, z)-plane across the second peak position in the x direction for (*a*i–*b*i) no control, (*a*ii–*b*ii) $y_d^+ = 15$ control and (*a*iii–*b*iii) $y_d^+ = 28$ control at $t^+ = 10$. Red (light) or solid line, $v' > 0$; blue (dark) or dashed line, $v' < 0$.

around $y^+ = 20$, and the two extreme-value positions are located at $y^+ = 9$ and $y^+ = 35$, respectively. The above analysis is confirmed by figures 6(*b*i) and 7(*b*i), which show the contours of v' on the (y, z)-plane across the second peak position in the x direction at $t^+ = 10$ and $t^+ = 20$, respectively. Although, as time progresses, v' deflects in the z direction, it is still obvious that v' changes sign around $y^+ = 20$, and reaches extreme values near $y^+ = 9$ and $y^+ = 35$, respectively.

Distributions of v' at $t^+ = 10$ and 20 under the $y_d^+ = 15$ and 28 controls are also shown in figures 6 and 7, respectively. Evidently, the $y_d^+ = 15$ control weakens v' below $y^+ = 20$, whereas the $y_d^+ = 28$ control strengthens it. This phenomenon may be explained by the wall-normal distribution of v'. It has been shown that v' changes sign in the y direction around $y^+ = 20$. If the detection plane is located at $y_d^+ = 15$, the blowing/suction velocity on the wall determined by the opposition-control scheme is in the opposite direction to v' below $y^+ = 20$. In this sense, the $y_d^+ = 15$ control

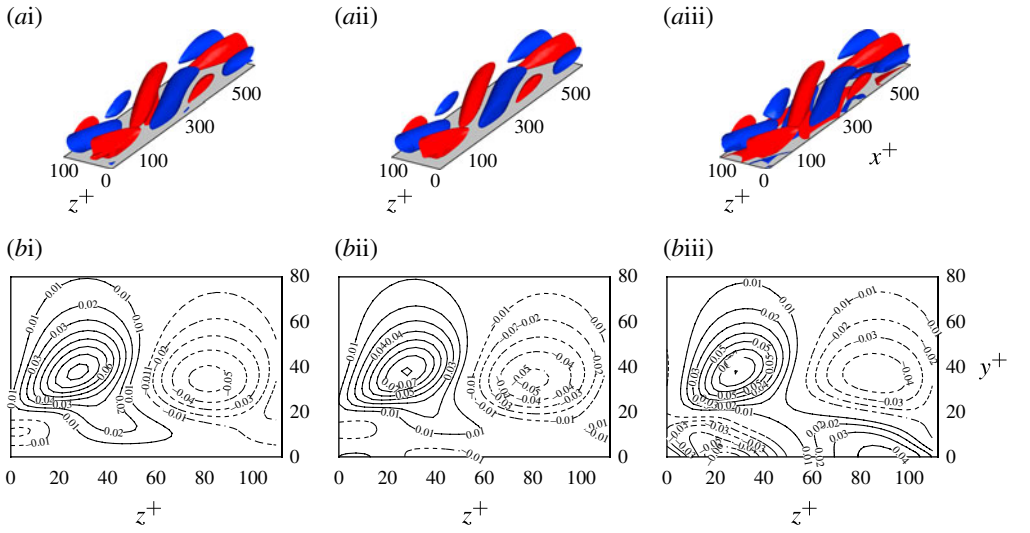

FIGURE 7. (Colour online) (*ai*–*aiii*) Iso-surface of $|v'| = 0.02$ and (*bi*–*biii*) contours of v' on the (y, z)-plane across the second peak position in the x direction at $t^+ = 20$. For the legend, see figure 6.

is a kind of out-of-phase control, and hence weakens v' below $y^+ = 20$, as shown in figures 6(*b*ii)–7(*b*ii). However, when the detection plane is moved to $y_d^+ = 28$, the blowing/suction velocity on the wall is strong and its direction is the same as that of v' below $y^+ = 20$. Hence, it is a kind of in-phase control and could enhance v' below $y^+ = 20$, as verified in figures 6(*b*iii)–7(*b*iii).

The $\partial u'/\partial x$ responsible for the vortex stretching in the next stage is a simple consequence of low-speed streak waviness generated naturally by the transient growth of the STG perturbation. In the early STG stage, $\partial u'/\partial x$ mainly results from the linear term $-(\partial w'/\partial x)(\partial U/\partial z)$, and hence varies with x and z in the form of $\cos(\alpha x)\sin(\beta z)$, as explained above. By the continuity constraint, v' just follows the variation of $\partial u'/\partial x$. The iso-surface of v' at $t^+ = 10$ shown in figure 6 confirms the above analysis. As time goes on, u' is quickly amplified and $w'\partial u'/\partial z$ reaches the amplitude of 0.9 at the end of the STG stage, $t^+ = 20$, whereas the linear term $w'\partial U/\partial z$ still keeps the early-time value around 0.5. Hence, the nonlinear term cannot be neglected any more than the linear term in (4.1). The nonlinear term $w'\partial u'/\partial z$ contributes to u' in the form of $\sin(\alpha x)\sin(\alpha x)\cos(\beta z)$; together with the contribution from $w'\partial U/\partial z$ in the form of $\sin(\alpha x)\sin(\beta z)$, it deflects the distribution of $\partial u'/\partial x$ in the z direction. As shown in figure 7, the iso-surface of v', a proxy for $\partial u'/\partial x$, evidently deflects in the z direction at $t^+ = 20$.

Figure 8 shows the distribution of $\partial u'/\partial x$ on the same (y, z)-plane at $t^+ = 10$ and 20 for the no-control and the two opposition-control cases. Notably, on this plane only positive $\partial u'/\partial x$ is meaningful in the sense that it contributes favourably to vortex stretching. At $t^+ = 10$, the $y_d^+ = 15$ control makes very little difference to the distribution of $\partial u'/\partial x$, compared with the no-control case. However, the $y_d^+ = 28$ control strengthens the near-wall waviness of the streak. At $t^+ = 20$, the distribution of $\partial u'/\partial x$ under $y_d^+ = 15$ control still keeps a pattern similar to that in the no-control case, but the magnitude in the positive region is obviously reduced. By the $y_d^+ = 28$ control, the magnitude of positive $\partial u'/\partial x$ is greatly enhanced, and the peak position moves

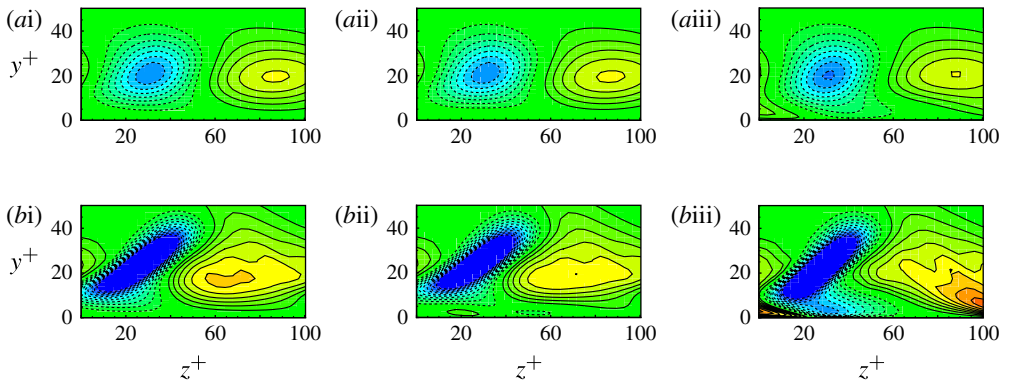

FIGURE 8. (Colour online) Contours of $\partial u'/\partial x$ on the (y, z)-plane at (*a*i–*a*iii) $t^+ = 10$ and (*b*i–*b*iii) $t^+ = 20$ for (*a*i–*b*i) no control, (*a*ii–*b*ii) $y_d^+ = 15$ control, and (*a*iii–*b*iii) $y_d^+ = 28$ control. Solid lines show positive contours and dashed lines show negative contours, with a contour level increment of 0.1.

closer to the wall, compared with the other two cases. These different behaviours of $\partial u'/\partial x$ under control with different detection locations may also be explained by the wall-normal distribution of v'. The above analysis shows that $\partial u'/\partial x \sim \partial w'/\partial z$, and according to the continuity equation $\partial v'/\partial y \sim -\partial u'/\partial x$. The $y_d^+ = 15$ control weakens v' below $y^+ = 20$, and $\partial v'/\partial y$ also becomes smaller than the no-control case, as does $\partial u'/\partial x$. For the $y_d^+ = 28$ control, the strengthened v' below $y^+ = 20$ makes $\partial v'/\partial y$ larger than the no-control case, and hence $\partial u'/\partial x$ is amplified.

Consider the influence of control on ω_x. According to Schoppa & Hussain (2002), the transient growth of STG perturbations could lead to the formation of a z-localized sheet of streamwise vorticity ω_x. The evolution of streamwise vorticity ω_x may be described by

$$\frac{\partial \omega_x}{\partial t} = \underbrace{-u\frac{\partial \omega_x}{\partial x}}_{\text{ADX}} \underbrace{-v\frac{\partial \omega_x}{\partial y}}_{\text{ADY}} \underbrace{-w\frac{\partial \omega_x}{\partial z}}_{\text{ADZ}} + \underbrace{\frac{\partial v}{\partial x}\frac{\partial u}{\partial z}}_{\text{TI1}} \underbrace{-\frac{\partial w}{\partial x}\frac{\partial u}{\partial y}}_{\text{TI2}} + \underbrace{\omega_x\frac{\partial u}{\partial x}}_{\text{ST}}, \tag{4.7}$$

in which ADX, ADY and ADZ denote the advection terms due to u, v and w, TI1 and TI2 represent the contributions from tilting, and ST represents that from stretching, respectively. For linear perturbations, the generation of the ω_x sheet is dominated by the tilting term TI2, whereas the TI1 and ST terms are not important, as described by Schoppa & Hussain (2002). For the present finite-amplitude perturbations, the magnitudes of the terms in (4.7) are first checked. TI2 still dominates over other terms in the STG stage. For example, at $t^+ = 10$, the maximum amplitude of TI2 is around 3.1, whereas those of TI1 and ST are approximately 0.18 and 0.64. At the end of the first stage, $t^+ = 20$, TI2 decreased to 2.9, and TI1 and ST both increased to 0.91 and 1.5, respectively. TI2 could be further decomposed into linear and nonlinear parts, $-(\partial w'/\partial x)(\partial U/\partial y)$ and $-(\partial w'/\partial x)(\partial u'/\partial y)$. The linear part is approximately 6 and 4 times larger than the nonlinear part at $t^+ = 10$ and 20, respectively. Hence, generation of the ω_x sheet by the STG mechanism could still be considered as a linear process. However, the nonlinear effects take up more and more partitions over time.

The streak vortex line coordinate system (x, n, s) is chosen to analyse the linear evolution process of the streamwise vorticity perturbation ω_x', as done by Schoppa &

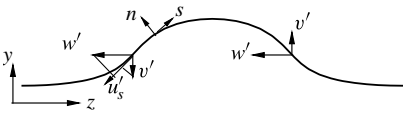

FIGURE 9. Schematic plot of streak vortex line coordinates.

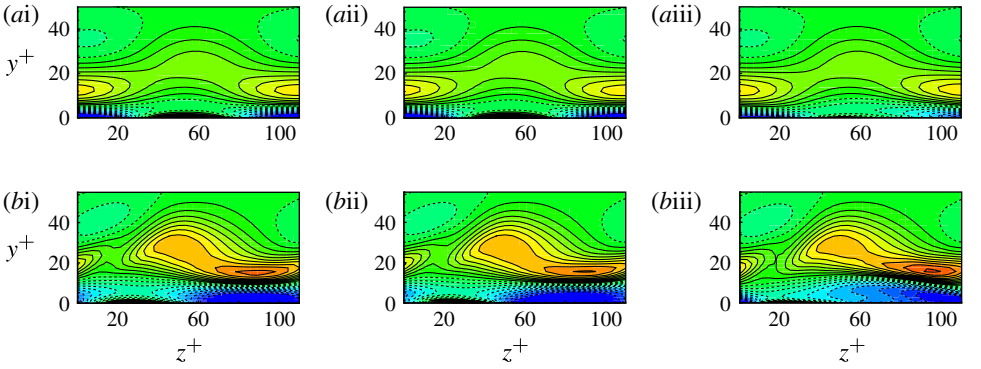

FIGURE 10. (Colour online) Contours of ω_x on the (y, z)-plane at (*a*i–*a*iii) $t^+ = 10$ and (*b*i–*b*iii) $t^+ = 20$ for (*a*i–*b*i) no-control, (*a*ii–*b*ii) $y_d^+ = 15$ control, and (*a*iii–*b*iii) $y_d^+ = 28$ control. Contour levels are from -3 to 3 in increments of 0.3. Solid lines show positive contours and dashed lines show negative contours.

Hussain (2002). The coordinates are schematically shown in figure 9; recall that both the base-flow velocity U and vorticity Ω are single-component, i.e. $\boldsymbol{u} = U(n)\boldsymbol{x}$ and $\boldsymbol{\omega} = \Omega(n, s)\boldsymbol{s}$ in this coordinate system. The linearized inviscid evolution equation for streamwise vorticity perturbation ω_x' can be written as ((14a) in Schoppa & Hussain 2002)

$$\frac{\partial \omega_x'}{\partial t} + U\frac{\partial \omega_x'}{\partial x} = \Omega\frac{\partial u_s'}{\partial x}, \tag{4.8}$$

in which u_s' is the velocity component tangential to the vortex line, as shown in figure 9. Initially, $v' = 0$ and u_s' primarily stem from the projection of w'. Because of the sinusoidal x-variation of w' and since Ω is much greater near the streak trough than near the streak crest, ω_x' is first generated in the streak trough region at the streamwise position corresponding to the zero-crossing point of w', and is then advected in the streamwise direction by the mean flow. With increasing time, ω_x' can also be generated at the streak flank and crest, and forms a z-continuous sheet (Schoppa & Hussain 2002). In the STG stage, v' is gradually developed. If v' is negative near the left trough of the streak and positive near the right trough, as shown in figure 9, it will result in a favourable contribution to u_s' and vice versa.

Figure 10 shows the distribution of ω_x' on the (y, z)-plane through the zero-crossing position of w' at $t^+ = 10$ and 20 for the no-control and the two control cases, respectively. In all three cases, a flat, z-localized elliptical patch of positive ω_x' is formed in the streak trough region at $t^+ = 10$, as described by Schoppa & Hussain (2002). At $t^+ = 20$, ω_x' is also pronounced at the streak flank and crest. The influence

of control on the elliptical patch of ω_x' in the streak trough region, which will be stretched into a streamwise vortex in the post-STG stage, is not obvious at $t^+ = 10$, but can be distinguished at $t^+ = 20$. At both $t^+ = 10$ and 20, the distribution of v' displays a negative region near the left trough and a positive region near the right trough of the streak for all three cases, but with different magnitudes, as shown in figures 6 and 7. The $v' < 0$ region near the left trough and the $v' > 0$ region near the right trough are suppressed by the $y_d^+ = 15$ control, but greatly enhanced by the $y_d^+ = 28$ control. At $t^+ = 10$, because $\partial v'/\partial x$ is negligible near the streamwise location where w' is zero and $\partial w'/\partial x$ takes the maximum value, the distribution of ω_x' on the plane at this streamwise position is unable to reveal the influence of the controls, as shown in figure 10(*a*i–*a*iii). At $t^+ = 20$, however, the $y_d^+ = 15$ control and the $y_d^+ = 28$ control work together with the increased overlapping of the v' and w' distribution in the streamwise direction, resulting in the attenuation and magnification of ω_x', respectively, as verified by comparing figure 10(*b*ii,*b*iii) with figure 10(*b*i).

The influence of control on the ω_x' very close to the wall is obvious: the magnitude of ω_x' is dramatically attenuated below $y^+ = 5$ by the $y_d^+ = 28$ control at both $t^+ = 10$ and 20, as shown in figure 10(*a*iii,*b*iii). For the no-control case, the negative ω_x' regions underneath the positive ω_x' and closer to the wall are a kinematic consequence of the wall no-slip condition, and are mainly composed of $\partial w'/\partial y < 0$. In the case of the $y_d^+ = 28$ control, v' near the wall is considerably strengthened, as depicted in figures 6(*b*iii) and 7(*b*iii), generating $\partial v'/\partial z > 0$ in the middle and $\partial v'/\partial z < 0$ near the two sides of the domain in the z direction. This counteracts the effect of $\partial w'/\partial y$, resulting in the attenuation of ω_x' near the wall. Notably, although the vorticity adjacent to the wall is suppressed by the $y_d^+ = 28$ control, the streamwise vortices generated later are not weakened compared with the no-control case, indicating that the lift-up mechanism described by Koumoutsakos (1997) for the two-dimensional vortex dipole is not dominant in the present three-dimensional vortex generation process.

4.2. *The post-STG stage*

After the transient growth in the STG stage, the nonlinear effects are triggered by the greatly amplified perturbations and play an important role in the post-STG stage. The streamwise vortices are generated by directly stretching the previously produced, z-localized vorticity sheet, and the advection and tilting are not important in this process (Schoppa & Hussain 2002). However, in the control cases, wall blowing and suction alter the near-wall distribution of v' and w', which are directly related to the advection and tilting contributions to ω_x. Therefore it is necessary to check whether the dominance of ST over other terms is changed by the control. If it is, then what is the new dominator? If it is not, how does the control take effect through ST?

The inviscid evolution equation for streamwise vorticity ω_x, (4.7), is employed to investigate how the control influences the vortex formation in this nonlinearity-dominated stage. Notably, according to (4.7), only the terms that have the same sign as that of ω_x at the same place can result in a favourable contribution to the generation of streamwise vortices. ADX only advects ω_x in the streamwise direction; as such, it is not important to the generation of streamwise vortices. Therefore, only the spatial correspondence of ADY, ADZ, TI1, TI2 and ST with streamwise vorticity ω_x are carefully checked. The vortices at $t^+ = 40$ are studied first. Neither the ADY nor the ADZ regions are in coincidence with the regions possessed by ω_x with the same sign in the uncontrolled flow. The situations for the two control cases are similar to the no-control case, suggesting that regardless of whether control is applied or not, the advection terms are not dominant in the generation of streamwise vortices. Compared

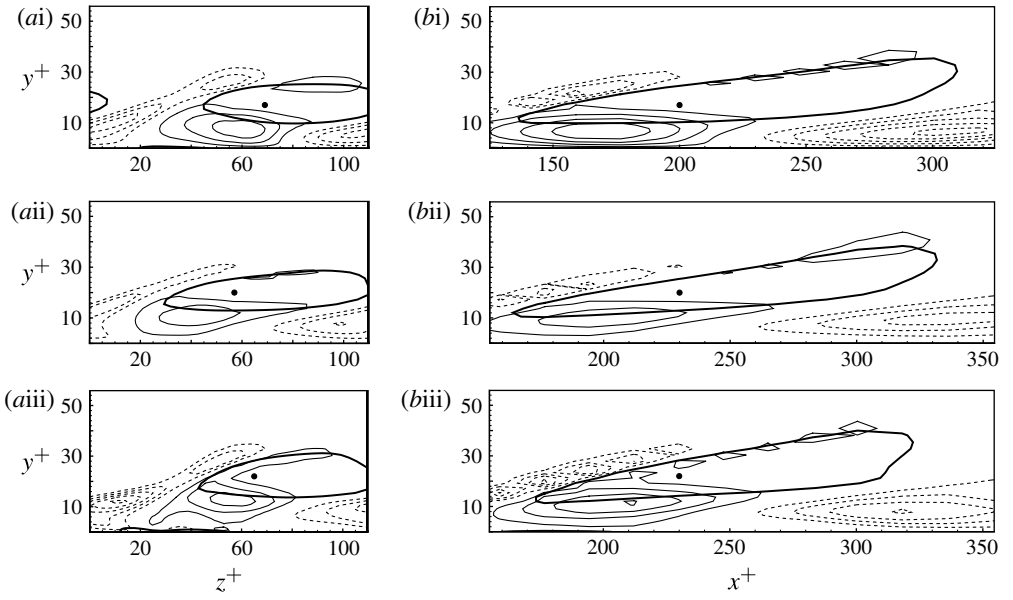

FIGURE 11. Contours of TI2 on (*a*i–*a*iii) the (y, z)-plane and (*b*i–*b*iii) the (x, y)-plane across the vortex core at $t^+ = 40$ for (*a*i–*b*i) no control, (*a*ii–*b*ii) $y_d^+ = 15$ control, and (*a*iii–*b*iii) $y_d^+ = 28$ control. The bold solid line is the iso-contour of $\omega_x = 2$, which identifies the vortex-related $\omega_x > 0$ region. The black dot shows the position of the vortex core. The thin solid lines depict positive TI2, and the thin dashed lines represent negative TI2 with contour level increments of 1.

with the other terms, TI1 is too small to be taken into account. Detailed analysis is conducted for the tilting term TI2, which plays an important role in producing the ω_x sheet in the STG stage, and the stretching term ST, which is considered to be directly responsible for the generation of streamwise vortices by Schoppa & Hussain (2002). The contours of TI2 and ST on the (y, z)-plane and (x, y)-plane across the vortex core are depicted in figures 11 and 12.

At $t^+ = 40$, the core of the vortex with positive ω_x identified by the position of minimum λ_2, is located at (200, 17, 69) for the no-control case, (230, 20, 57) for $y_d^+ = 15$ control, and (230, 22, 65) for $y_d^+ = 28$ control: see figure 3(*a*i–*a*iii) for reference. In figures 11 and 12, the vortex cores are denoted by black dots. The bold lines identify the vortex-related $\omega_x > 0$ regions, and the thin lines stand for the terms concerned (solid for positive values and dashed for negative values). The distribution of TI2 shows that although the $\omega_x > 0$ region remains enclosed by the positive TI2 region, it has already moved to a marginal area. In all three cases, the cores of the positive TI2 are located underneath the elevated streamwise vortices. Notably, the TI2 term, responsible for the creation of the ω_x sheet in the streak trough region in the STG stage, as discussed in the previous section, gradually weakens its influence on streamwise vortex generation in this nonlinearity-dominated stage. The distribution of ST is shown in figure 12. The positive ST is consistently in good spatial accordance with the positive ω_x region on both the (y, z)-plane and the (x, y)-plane for both the no-control and the two control cases, indicating that the control cannot change the dominant position of ST in the formation of streamwise vortices. ST is obviously weakened by the $y_d^+ = 15$ control; the magnitude of ST is not drastically changed

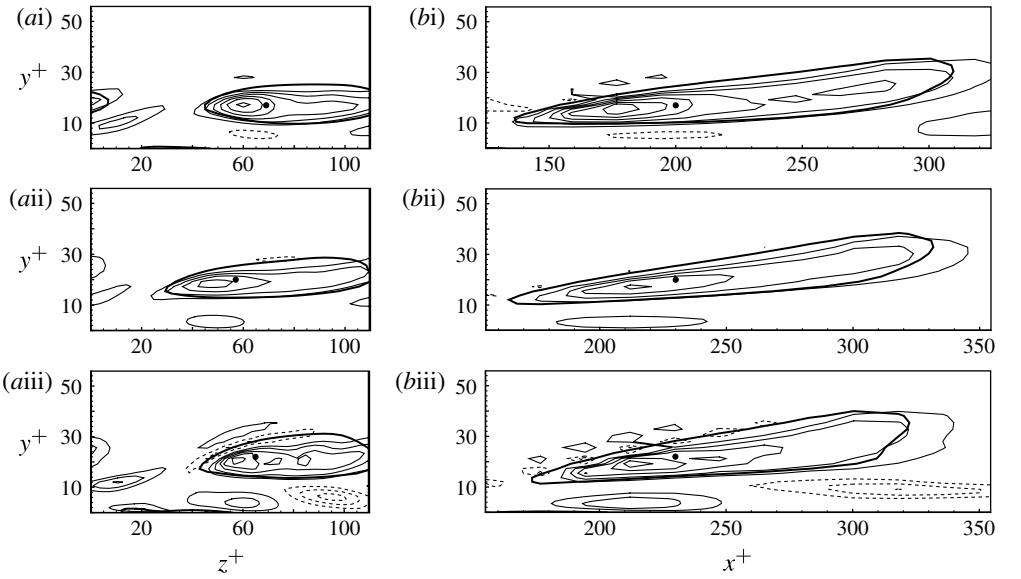

FIGURE 12. Contours of ST on (*a*i–*a*iii) the (y, z)-plane and (*b*i–*b*iii) the (x, y)-plane across the vortex core at $t^+ = 40$ for (*a*i–*b*i) no control, (*a*ii–*b*ii) $y_d^+ = 15$ control, and (*a*iii–*b*iii) $y_d^+ = 28$ control. The bold solid line is the iso-contour of $\omega_x = 2$, which identifies the vortex-related $\omega_x > 0$ region. The black dot shows the position of the vortex core. The thin solid lines depict positive ST, and the thin dashed lines represent negative ST with contour level increments of 0.5.

by the $y_d^+ = 28$ control, but multiple extreme points appear within the vortex-related $\omega_x > 0$ region. The spatial correspondence between streamwise vortices, and TI2 and ST, at the later time $t^+ = 65$ and 88 are also checked. At $t^+ = 88$, the regions with pronounced TI2 are almost completely separated from those occupied by streamwise vortices; the regions with significant ST almost completely reside in streamwise vortices for both the no-control and the two control cases. Therefore, the dominant position of ST over other terms in streamwise vortex generation is not changed by the control, regardless of where the detection planes are located.

The attenuation of ST by the $y_d^+ = 15$ control is easily understood, according to the analysis of the production of the streamwise vorticity sheet in the previous section. The stretching term ST is the product of ω_x and $\partial u/\partial x$. Via the $y_d^+ = 15$ control, ω_x generated at the end of the STG stage is smaller than that in the no-control case, and $\partial u/\partial x$ is also slightly suppressed; these two effects cause the direct attenuation of the ST term. The alleviated stretching effect weakens the production of streamwise vorticity, and iteratively, ω_x under $y_d^+ = 15$ control does not have the opportunity to grow as much as that in the no-control case. For the $y_d^+ = 28$ control, ω_x and $\partial u/\partial x$ produced in the STG stage are both stronger than those in the no-control case; however, no obvious enhancement in ST is observed in the post-STG stage at $t^+ = 40$ (the maximum ST for the no-control case is 4.0, for the $y_d^+ = 15$ control it is 2.2, and for the $y_d^+ = 28$ control 4.1). In addition, at $t^+ = 88$, it is even smaller than the no-control case (the maximum ST for the no-control case is 7.1, for the $y_d^+ = 15$ control it is 2.6, and for the $y_d^+ = 28$ control 5.6). This implies that control in the post-STG stage exhibits different effects from that in the STG stage. In order to clarify the roles played by control, controls with different detection locations are imposed

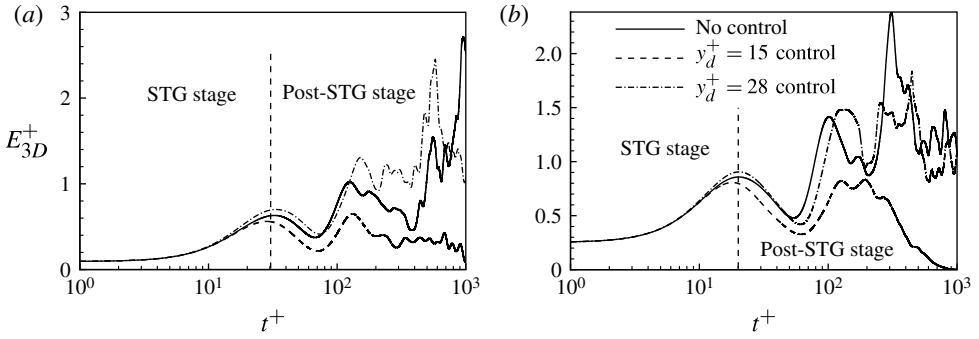

FIGURE 13. Time evolution of E_{3D} under no control and opposition control with initial $\theta_{20} = 50°$: (*a*) $w_{rms}^+ = 0.3$ and (*b*) $w_{rms}^+ = 0.5$.

at different stages, and their influence on the generation and evolution of streamwise vortices is discussed in the following section.

5. Effects of control imposed at different stages

The conclusions drawn in § 4 are validated by simulations with different initial conditions. Figure 13 shows the time evolution of perturbation energy E_{3D} with initial $\theta_{20} = 50°$ and $w_{rms}^+ = 0.3$ and 0.5, which can be compared with figure 2 for the cases with initial $\theta_{20} = 45°$ and $w_{rms}^+ = 0.5$. Starting from all the initial conditions considered in the present study, the perturbation energy experiences a similar time history. The transient growth stage lasts until a later time at $t^+ = 30$ for the smaller initial perturbation $w_{rms}^+ = 0.3$. For the larger initial perturbation $w_{rms}^+ = 0.5$, the temporal instant defining the end of the STG stage remains at $t^+ = 20$ for the current $\theta_{20} = 50°$, similar to those in the $\theta_{20} = 45°$ case. This is consistent with the result of Park, Hwang & Cossu (2011), who noted that the time needed to reach the maximum energy growth decreases as the initial perturbation energy increases. The responses of v', $\partial u/\partial x$, and ω_x in the STG stage, as well as TI2 and ST in the post-STG stage, to the controls with $\theta_{20} = 50°$ are also similar to those with $\theta_{20} = 45°$, and will not be described again here. In the following, all analyses of the minimal channel flow are based on the initial conditions with $\theta_{20} = 50°$ and $w_{rms}^+ = 0.3$.

In order to distinguish the effect of control in the STG stage from that in the post-STG stage, controls that are only applied in $0 < t^+ < 30$ (STG control), $t^+ > 30$ (post-STG control), and $t^+ > 0$ (full-time control) are performed with $y_d^+ = 15$ and 28, respectively. The streamwise vortices at different times during $60 < t^+ < 240$ under different controls are carefully scrutinized, as discussed below.

Figure 14 shows the evolution of streamwise vortices under various controls with $y_d^+ = 15$, and those in the no-control case are also shown for comparison. Vortical structures in the no-control and full-time control cases with current initial conditions are similar to those with $\theta_{20} = 45°$ and $w_{rms}^+ = 0.5$ shown in figure 3. With increasing time, streamwise vortices are generated and gradually elongated in the streamwise direction, and arc heads appear and form hairpin-like structures in the no-control case; the full-time $y_d^+ = 15$ control greatly inhibits the growth of streamwise vortices. The STG control is compared with the no-control case in figures 14(*a*iii–*e*iii) and 14(*a*i–*e*i). Out-of-phase control with $y_d^+ = 15$ attenuates the generation of ω_x and $\partial u'/\partial x$ in the STG stage; as such, ST is weaker and the streamwise vortices are obviously attenuated

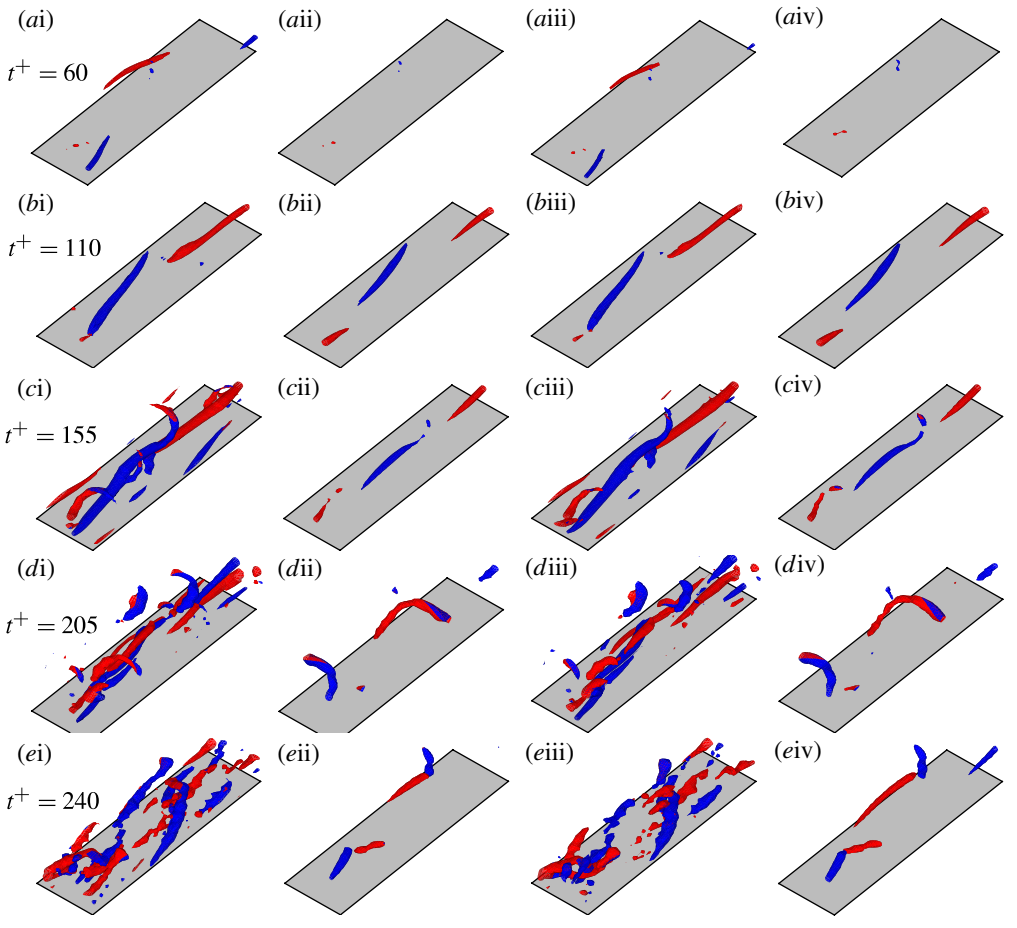

FIGURE 14. (Colour online) Iso-surface of $\lambda_2 = -2$ at (*a*i–*a*iv) $t^+ = 60$, (*b*i–*b*iv) $t^+ = 110$, (*c*i–*c*iv) $t^+ = 155$, (*d*i–*d*iv) $t^+ = 205$ and (*e*i–*e*iv) $t^+ = 240$ for (*a*i–*e*i) no control, (*a*ii–*e*ii) full-time control, (*a*iii–*e*iii) STG control, and (*a*iv–*e*iv) post-STG control with $y_d^+ = 15$. Red (light), $\omega_x > 0$; blue (dark), $\omega_x < 0$.

earlier in the stretching process ($t^+ = 60$) compared with the no-control case. The influence of STG control becomes weaker as time progresses, and after $t^+ = 155$, these structures under STG control are similar to those in the no-control case. When the post-STG control and no-control cases are compared, as in figure 14(*a*iv–*e*iv) and 14(*a*i–*e*i), post-STG control can also successfully suppress streamwise vortices. However, due to the absence of the attenuation of ω_x and $\partial u'/\partial x$ in the STG stage, the vortices under post-STG control are slightly stronger than those under full-time control in figure 14(*a*ii–*e*ii). Therefore, for $y_d^+ = 15$, STG control and post-STG control are both favourable in attenuating streamwise vortices.

Vortical structures under $y_d^+ = 28$ controls, applied in different stages, are shown in figure 15. The performance of full-time control with $\theta_{20} = 50°$ and $w_{rms}^+ = 0.3$ is also similar to that with $\theta_{20} = 45°$ (figure 3). Here, vortical structures are stronger under control early in the stretching process, and increase in number later, when compared with the no-control case. The influence of STG control and post-STG

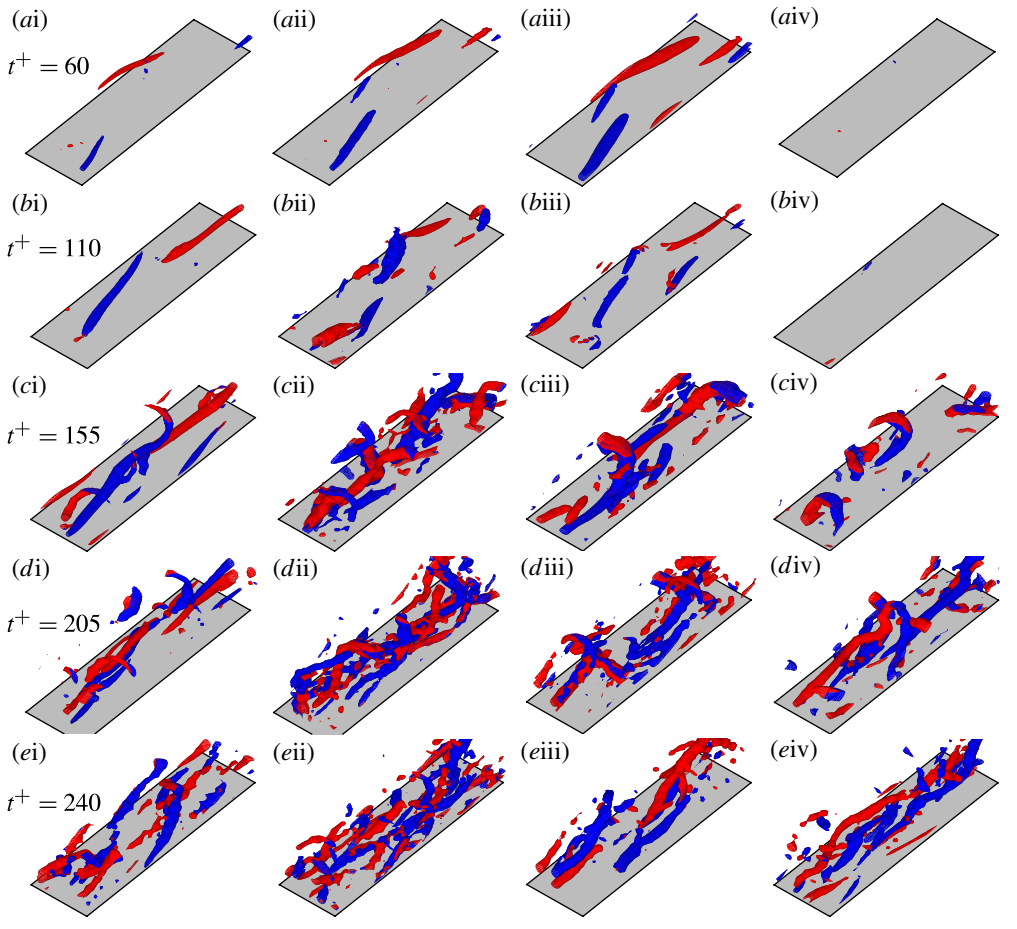

FIGURE 15. (Colour online) Iso-surface of $\lambda_2 = -2$ at (*a*i–*a*iv) $t^+ = 60$, (*b*i–*b*iv) $t^+ = 110$, (*c*i–*c*iv) $t^+ = 155$, (*d*i–*d*iv) $t^+ = 205$ and (*e*i–*e*iv) $t^+ = 240$ for (*a*i–*e*i) no control, (*a*ii–*e*ii) full-time control, (*a*iii–*e*iii) STG control, and (*a*iv–*e*iv) post-STG control with $y_d^+ = 28$. Red (light), $\omega_x > 0$; blue (dark), $\omega_x < 0$.

control are shown in figures 15(*a*iii–*e*iii) and 15(*a*iv–*e*iv). At $t^+ = 60$, vortices are notably strengthened by STG control, and are greatly weakened by post-STG control, compared with the vortices in both the no-control and full-time control cases. The different roles that control plays in the STG stage and post-STG stage are clearly exposed by this comparison. In the STG stage, the in-phase control with $y_d^+ = 28$ promoted the production of ω_x and $\partial u'/\partial x$ (figures 8 and 10), therefore enhancing the stretching effect, resulting in strengthened vortical structures. For example, at $t^+ = 60$, the maximum amplitude of the ST term in the no-control, full-time control, STG control, and post-STG control cases are 2.21, 2.58, 3.54 and 1.56, respectively. As soon as the vortices are generated, the opposite blowing/suction applied on the wall counteracts the sweep and ejection motions caused by streamwise vortices (Choi *et al.* 1994). Therefore, whether the detection plane is located at $y^+ = 15$ or $y^+ = 28$, opposition control in the post-STG stage favours the attenuation of streamwise vortices. The full-time $y_d^+ = 28$ control combines the opposite effects to STG control and post-STG control, under which the vortical structures are stronger

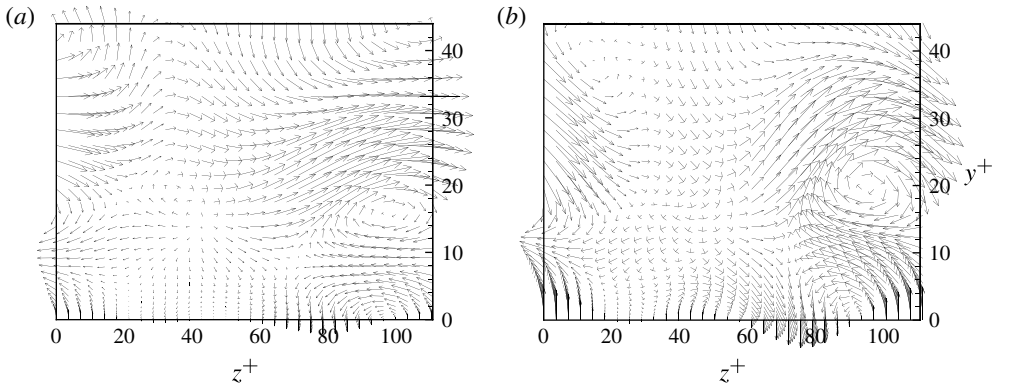

FIGURE 16. (v, w) vectors on the (y, z)-plane across the core of the positive streamwise vortex at $t^+ = 60$: (*a*) $y_d^+ = 15$ full-time control; (*b*) $y_d^+ = 28$ full-time control.

than post-STG control and weaker than STG control. At later times ($t^+ = 205$ and 240), new streamwise vortices are regenerated by the post-STG $y_d^+ = 28$ control, while the control with $y_d^+ = 15$ remains very effective in attenuating streamwise vortices. In order to understand this different behaviour, velocity vectors on the (y, z)-plane across the core of the positive streamwise vortices under $y_d^+ = 15$ and 28 control are examined. Figure 16 shows that the vertical velocity signals detected at $y^+ = 15$ and 28 are of the same sign but different magnitude, indicating that proper control strength in the post-STG stage is also significant for achieving sustained vortex suppression.

Control imposed at different stages confirms the importance of STG to streamwise vortex generation. The $y_d^+ = 28$ in-phase control can result in vortex augmentation, while the $y_d^+ = 15$ out-of-phase control is beneficial to the attenuation of streamwise vortices. In addition, the effect of post-STG control is closely related to control strength.

Notably, v' at $y^+ = 10$ is of the same sign as that at $y^+ = 15$ and almost reaches the maximum amplitude in the STG stage (figures 6 and 7). If the above analysis is true, the out-of-phase control with $y_d^+ = 10$ will be more effective than that with $y_d^+ = 15$ in suppressing the generation of the ω_x sheet and the subsequent streamwise vortices. To validate this assertion, the opposition controls are performed with $y_d^+ = 10$ applied in full time, only in the STG stage and only in the post-STG stage, as shown in figure 17. The attenuation of streamwise vortices by $y_d^+ = 10$ STG control in figure 17(*a*iii) is heavier than that by the $y_d^+ = 15$ STG control in figure 14(*a*iii), compared with the no-control case in figure 17(*a*i). When the STG stage is left free of control, the post-STG $y_d^+ = 10$ control is not as effective as the $y_d^+ = 15$ control shown in figure 14(*a*iv–*e*iv), although it still renders the streamwise vortices weaker than those in the no-control case, as shown in figure 17(*a*i–*e*i). As discussed, once the vortex is generated, v' at $y^+ = 10$ has the same sign as that at $y^+ = 15$, but with much lesser strength. The difference between the effects of the post-STG $y_d^+ = 10$ and $y_d^+ = 15$ control on attenuating streamwise vortices can be attributed to the differences in control strength.

6. Strengthened out-of-phase control and lessened in-phase control

The above analysis of the behaviour of control imposed at different stages shows that the $y_d^+ = 10$ control is superior to the $y_d^+ = 15$ control in the STG stage due

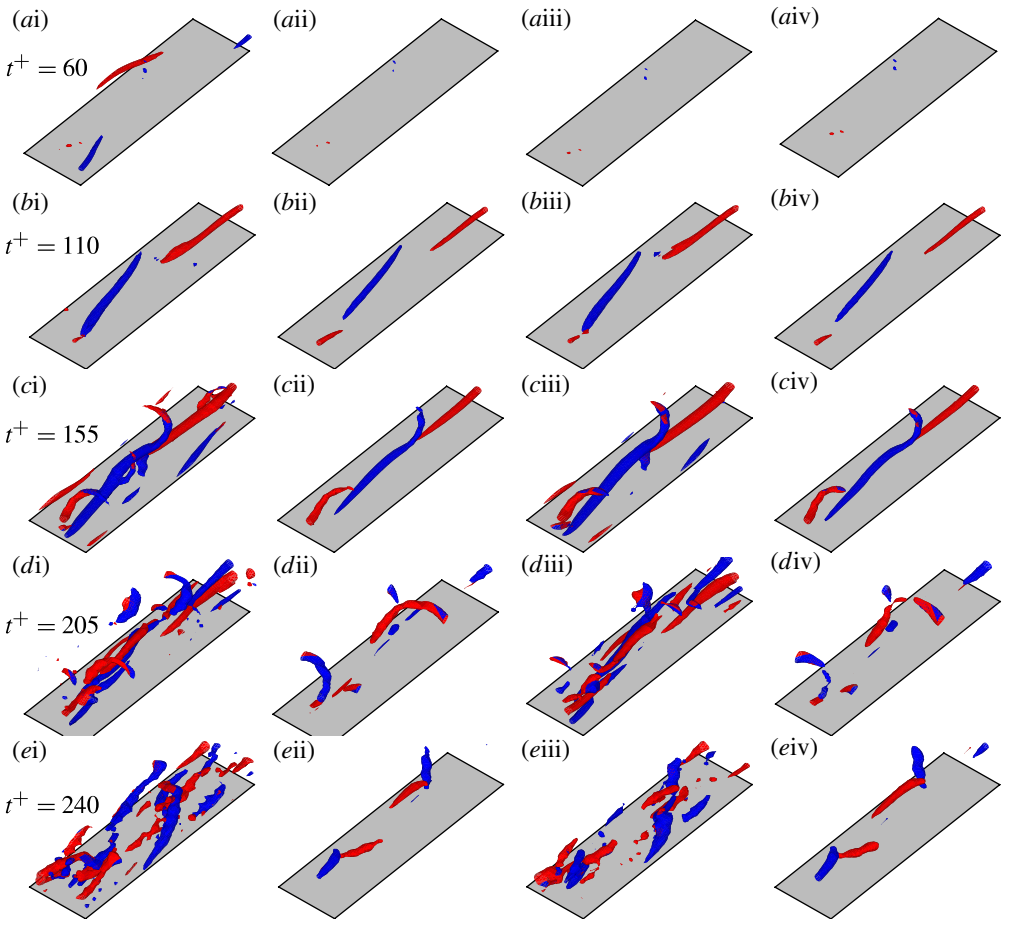

FIGURE 17. (Colour online) Iso-surface of $\lambda_2 = -2$ at (*a*i–*a*iv) $t^+ = 60$, (*b*i–*b*iv) $t^+ = 110$, (*c*i–*c*iv) $t^+ = 155$, (*d*i–*d*iv) $t^+ = 205$ and (*e*i–*e*iv) $t^+ = 240$ for (*a*i–*e*i) no control, (*a*ii–*e*ii) full-time control, (*a*iii–*e*iii) STG control, and (*a*iv–*e*iv) post-STG control with $y_d^+ = 10$. Red (light), $\omega_x > 0$; blue (dark), $\omega_x < 0$.

to its greater strength. On the other hand, the $y_d^+ = 10$ control is surpassed by the $y_d^+ = 15$ control after the STG stage due to its lesser strength. As a result, we devise a strengthened $y_d^+ = 10$ control by applying wall blowing/suction according to the amplified v' signal sensed at $y^+ = 10$. The vertical velocity imposed at the wall by the $y_d^+ = 28$ control is opposite in sign to that by the $y_d^+ = 15$ control in the STG stage; however, after the vortices are generated, the wall blowing/suction determined by the signals sensed at $y_d^+ = 15$ and 28 are of the same sign but with different strength, as shown in figure 16. The opposition control using the signal at $y_d^+ = 28$ but with a reduced strength can be reasonably assumed to also suppress turbulence through the attenuation of the extant streamwise vortices. The above analysis of the influence of the $y_d^+ = 28$ control in the STG stage is also in favour of the reduction of control strength. Therefore, the strengthened out-of-phase control and the lessened in-phase control are proposed as $v_{wall} = -Av_{y_d}$ with $A > 1$ for $y_d^+ < 15$ and $A < 1$ for $y_d^+ > 15$. Notably, Chung & Talha (2011) also extended the opposition control to $v_{wall} = -Av_{y_d}$; however, they set $A \leqslant 1$ for all the detection positions.

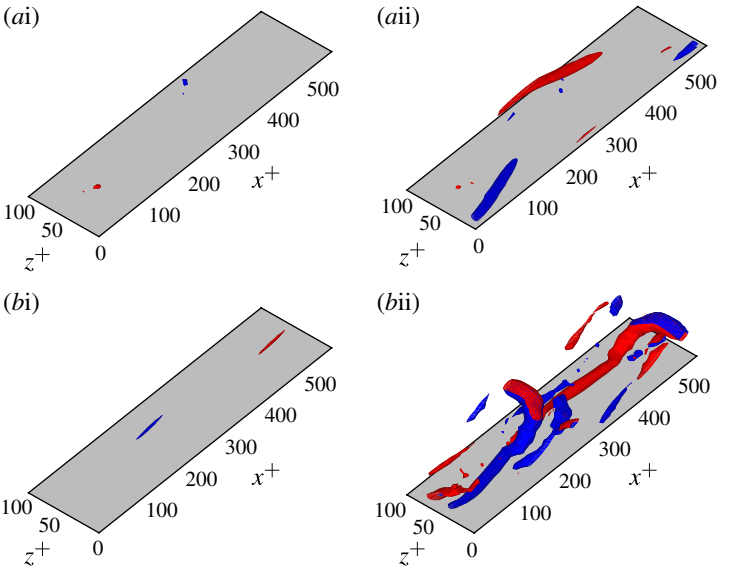

FIGURE 18. (Colour online) Iso-surface of (*a*i–*b*i) $\lambda_2 = -1.8$ for the strengthened $y_d^+ = 10$ control and (*a*ii–*b*ii) $\lambda_2 = -2$ for the lessened $y_d^+ = 28$ control at (*a*i–*a*ii) $t^+ = 60$ and (*b*i–*b*ii) $t^+ = 155$. Red (light), $\omega_x > 0$; blue (dark), $\omega_x < 0$.

The new extensions of the opposition-control scheme are first tested in the minimal channel flow. In the strengthened $y_d^+ = 10$ control, we set $A = 4$, while in the lessened $y_d^+ = 28$ control, we set $A = 0.3$. The vortical structures at $t^+ = 60$ and 155 under the newly proposed control schemes are shown in figure 18. Compared with the normal $y_d^+ = 10$ control, the superiority of the strengthened $y_d^+ = 10$ control is obvious in attenuating streamwise vortices, as seen in figures 17(*a*ii,*c*ii) and 18(*a*i,*b*i). Notably, the iso-surfaces of $\lambda_2 = -1.8$ are adopted for the strengthened $y_d^+ = 10$ control to show the much weaker vortical structures, while those of $\lambda_2 = -2$ were previously used for the normal $y_d^+ = 10$ control. The lessened $y_d^+ = 28$ control is also effective in weakening vortical structures compared with the no-control and the normal $y_d^+ = 28$ control cases, as seen in figures 18(*b*ii) and 15(*c*i,*c*ii). Figure 19(*a*) shows the time history of the plane-averaged wall skin friction under the normal $y_d^+ = 15$ and 28 control, the strengthened $y_d^+ = 10$ control, and the lessened $y_d^+ = 28$ control. Skin friction under the $y_d^+ = 15$ control is almost identical to that without control until $t^+ = 60$, at which the friction for the no-control case begins to increase notably while that under the $y_d^+ = 15$ control varies a little and then decays towards the level of laminar flow. Although the evolutions of E_{3D} under the $y_d^+ = 28$ control behave similarly to those in the no-control case (figure 2*a*), the skin friction is much larger than that without control from the beginning. The lessened $y_d^+ = 28$ control follows the curves of the no-control and the $y_d^+ = 15$ control cases when $t^+ < 60$, and then grows slightly higher than the no-control case until $t^+ = 260$. After that, it differs from the no-control case, and evolves towards the $y_d^+ = 15$ control case. The effectiveness of the strengthened $y_d^+ = 10$ control is displayed after $t^+ > 60$. Skin friction under the strengthened $y_d^+ = 10$ control decays and tends to the laminar state much faster than the normal $y_d^+ = 15$ control.

The strengthened $y_d^+ = 10$ control and the lessened $y_d^+ = 28$ control are also tested in the full-scale turbulent channel flow at $Re_\tau = 180$, and compared with the

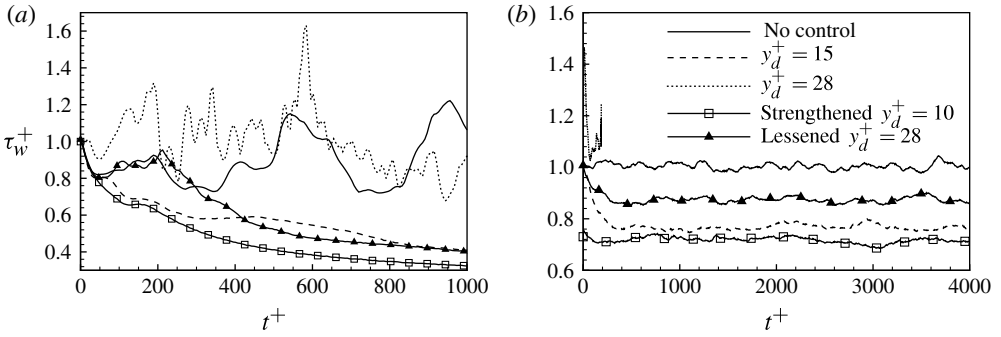

FIGURE 19. Time history of the plane-averaged wall shear stress: (*a*) minimal channel; (*b*) full-scale channel.

original $y_d^+ = 15$ control. A number of values of control strength are checked by adjusting parameter A from 0.1 to 8. For the strengthened $y_d^+ = 10$ control, the drag reduction rate is notably increased by increasing A from 1 to 4; after that, it gradually tends to a limit. At $A = 8$, the friction is reduced by approximately 29 % by the strengthened $y_d^+ = 10$ control, which is greater than the value of 25 % achieved by the original opposition control with $y_d^+ = 15$. For the lessened $y_d^+ = 28$ control, the optimal value of A is approximately 0.25 in terms of drag reduction rate, which is consistent with the findings of Chung & Talha (2011). At $A = 0.25$, the friction is reduced by approximately 12 % by the lessened $y_d^+ = 28$ control. Notably, the cases studied by Chung & Talha (2011) only correspond to the lessened in-phase control proposed here. By amplifying the control strength with the detection position below $y^+ = 15$, we obtain a larger drag reduction rate than that by the $y_d^+ = 15$ control, which was thought to be the best result that could be achieved by opposition control (Choi *et al.* 1994; Hammond *et al.* 1998; Chung & Talha 2011). Detailed analysis of more combinations of A and y_d^+ will be conducted in future work.

The root mean squares of velocity fluctuations and Reynolds shear stress are shown in figure 20 for the two new control schemes; those of the no-control and original $y_d^+ = 15$ control cases are also shown for comparison. The suppression of turbulence intensities and the Reynolds shear stress are remarkable for all three control cases. In all the profiles, those obtained by the strengthened $y_d^+ = 10$ control are the lowest, considerably lower than those obtained by the original $y_d^+ = 15$ control. This result is also in accordance with the drag reduction rate achieved by the various control schemes.

One more question, concerning the main conclusion drawn from the present study, requires further elucidation. The above analysis indicates that the effect of opposition control with different y_d^+ on streamwise vortices strongly depends on the position where v' changes sign. In the present study, STG perturbation is set to reach maximum value at $y^+ = 20$; therefore, the wall-normal velocity changes sign at this position, resulting in the opposite effects on ω_x production by the control sensing at $y_d^+ = 15$ and 28, respectively. The value of $y^+ = 20$ is not chosen arbitrarily; statistically, the cores of the streamwise vortices are located at approximately $y^+ = 20$, as evidenced by the second maximum position in the distribution of the root mean square of streamwise vorticity (see figure 4*b* in Kim *et al.* 1987). The choice of the present STG perturbation can ensure that the core of the generated vortices is located at

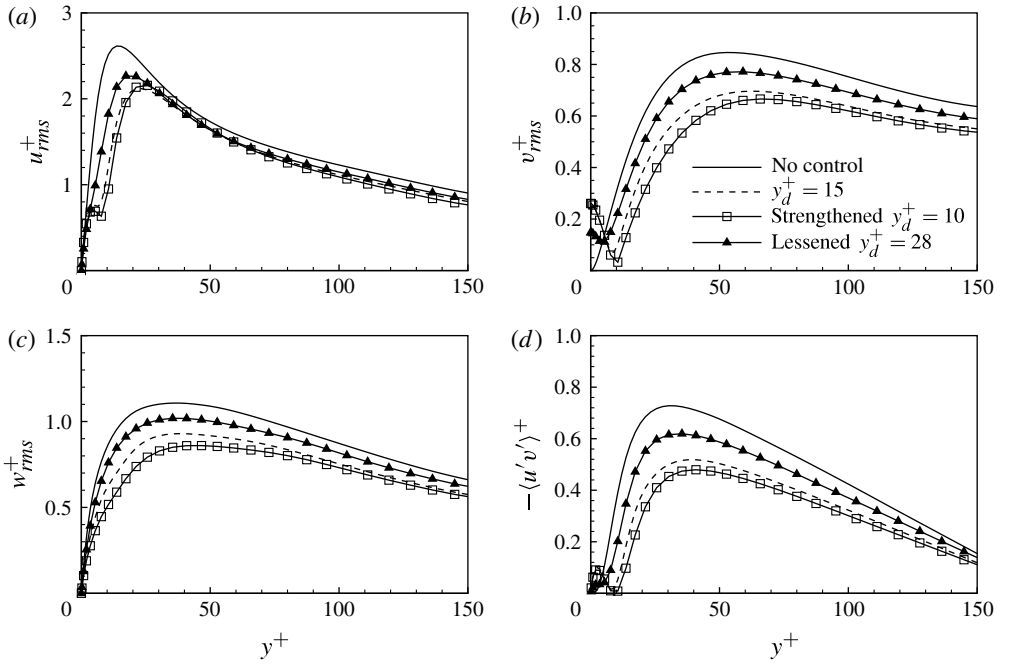

FIGURE 20. Turbulence intensities and Reynolds shear stress in a full-scale turbulent channel flow at $Re_\tau = 180$. (*a*) u^+_{rms}, (*b*) v^+_{rms}, (*c*) w^+_{rms}, and (*d*) $-\langle u'v'\rangle^+$. The quantities are non-dimensionalized by u_τ in the no-control case.

approximately $y^+ = 20$, as shown by figure 4(*c*). Therefore, the conclusion in the present work is meaningful in full-scale turbulence.

7. Summary and conclusion

The effect of opposition control on the STG-based generation of near-wall streamwise vortices is studied by direct numerical simulation of minimal channel flow at $Re_\tau = 180$. The normal-mode stable streaks with $\theta_{20} = 45$ and $50°$ are considered together with the initial STG perturbation at different magnitudes ($w^+_{rms} = 0.3$ and 0.5). The initially imposed STG perturbation is set to reach maximum value at $y^+ = 20$ to ensure that the generated streamwise vortices are near this position. According to the evolution of perturbation energy and vortical structures, the entire process is roughly divided into two stages: the STG stage and the post-STG stage. The analysis of the magnitude of various terms in the transport equations for perturbation velocity and streamwise vorticity in the STG stage indicates that the generation of streamwise vorticity remains able to be approximated by a linear process although the initial perturbation is of finite magnitude, while nonlinearity quickly grows in the formation of streak waviness represented by $\partial u/\partial x$.

In the STG stage, v' changes sign near $y^+ = 20$; hence, $y_d^+ = 15$ control can weaken v' below $y^+ = 20$, while $y_d^+ = 28$ control can strengthen v' there, resulting in the respective suppression and enhancement of the streamwise vorticity produced in the z-localized elliptical patch of the streamwise vorticity sheet. In the vortex generation stage, the stretching effect remains dominant over advection and tilting effects, regardless of whether or not control is imposed. Via the $y_d^+ = 15$ control, the

alleviated streamwise vorticity production in the STG stage takes effect directly in the suppression of the stretching term, and iteratively causing the sustained overall attenuation of streamwise vortex generation. Via the $y_d^+ = 28$ control, however, no obvious enhancement in the stretching term is observed, indicating that the mechanism for control influencing the generation of streamwise vortices is different in the STG and post-STG stages.

Controls that are only applied in the STG stage confirm that out-of-phase phase control ($y_d^+ = 10$ and 15) can suppress the generation of streamwise vortices, while in-phase control ($y_d^+ = 28$) can enhance it. Controls imposed only in the post-STG stage show that detections at both $y_d^+ = 15$ and 28 are in favour of attenuating the extant streamwise vortices. The regeneration of streamwise vortices later, by control with higher detection location, reveals the influence of control strength.

Based on this knowledge, an extension of the opposition-control scheme is proposed, i.e. the strengthened out-of-phase control ($y_d^+ = 10$) and the lessened in-phase ($y_d^+ = 28$) control. The new control schemes are tested in both minimal and full-scale channel flows. The strengthened $y_d^+ = 10$ control behaves even better in terms of drag reduction and turbulence suppression than the original $y_d^+ = 15$ control, which is usually considered the most effective in opposition controls with various detection positions.

The present study leaves a number of questions open. How hairpin vortices are formed and how the controls influence their evolution require further investigation. Increased combinations of detection position and control strength in the strengthened out-of-phase control must also be studied in more detail.

Acknowledgement

The work is supported by National Natural Science Foundation of China (Project No. 10925210).

REFERENCES

DEL ÁLAMO, J. C. & JIMÉNEZ, J. 2006 Linear energy amplification in turbulent channels. *J. Fluid Mech.* **559**, 205–213.

BERNARD, P. S., THOMAS, J. M. & HANDLER, R. A. 1993 Vortex dynamics and the production of Reynolds stress. *J. Fluid Mech.* **253**, 385–419.

BROOKE, J. W. & HANRATTY, T. J. 1993 Origin of turbulence-producing eddies in a channel flow. *Phys. Fluids* A **5**, 1011–1022.

CHOI, H., MOIN, P. & KIM, J. 1994 Active turbulence control for drag reduction in wall-bounded flows. *J. Fluid Mech.* **262**, 75–110.

CHUNG, Y. M. & TALHA, T. 2011 Effectiveness of active flow control for turbulent skin friction drag reduction. *Phys. Fluids* **23**, 025102.

COLLIS, S. S., JOSLIN, R. D., SEIFERT, A. & THEOFILIS, V. 2004 Issues in active flow control: theory, control, simulation, and experiment. *Prog. Aerosp. Sci.* **40**, 237–289.

CUI, G., ZHOU, H., ZHANG, Z. & SHAO, L. 2004 A new dynamic subgrid eddy viscosity model with application to turbulent channel flow. *Phys. Fluids* **16**, 2835–2842.

ENDO, T., KASAGI, N. & SUZUKI, Y. 2000 Feedback control of wall turbulence with wall deformation. *Intl J. Heat Fluid Flow* **21**, 568–575.

HAMILTON, J. M., KIM, J. & WALEFFE, F. 1995 Regeneration mechanisms of near-wall turbulence structures. *J. Fluid Mech.* **287**, 317–348.

HAMMOND, E. P., BEWLEY, T. R. & MOIN, P. 1998 Observed mechanisms for turbulence attenuation and enhancement in opposition-controlled wall-bounded flows. *Phys. Fluids* **10**, 2421–2423.

JEONG, J. & HUSSAIN, F. 1995 On the identification of a vortex. *J. Fluid Mech.* **285**, 69–94.

JIMÉNEZ, J. & MOIN, P. 1991 The minimal flow unit in near-wall turbulence. *J. Fluid Mech.* **225**, 213–240.

JIMÉNEZ, J. & PINELLI, A. 1999 The autonomous cycle of near-wall turbulence. *J. Fluid Mech.* **389**, 335–359.

JIMÉNEZ, J. & SIMENS, M. P. 2001 Low-dimensional dynamics of a turbulent wall flow. *J. Fluid Mech.* **435**, 81–91.

JOVANOVIC, M. R. & BAMIEH, B. 2005 Componentwise energy amplification in channel flows. *J. Fluid Mech.* **534**, 145–183.

KASAGI, N., SUZUKI, Y. & FUKAGATA, K. 2009 Microelectromechanical systems-based feedback control of turbulence for skin friction reduction. *Annu. Rev. Fluid Mech.* **41**, 231–251.

KIM, J. 2003 Control of turbulent boundary layers. *Phys. Fluids* **15**, 1093–1104.

KIM, J. 2011 Physics and control of wall turbulence for drag reduction. *Phil. Trans. R. Soc.* A **369**, 1396–1411.

KIM, J. & BEWLEY, T. R. 2007 A linear systems approach to flow control. *Annu. Rev. Fluid Mech.* **39**, 383–417.

KIM, J. & MOIN, P. 1986 Flow structures responsible for the bursting process. *Bull. Am. Phys. Soc.* **31**, 1716.

KIM, J., MOIN, P. & MOSER, R. D. 1987 Turbulence statistics in fully developed channel flow at low Reynolds number. *J. Fluid Mech.* **177**, 133–166.

KOUMOUTSAKOS, P. 1997 Active control of vortex–wall interactions. *Phys. Fluids* **9**, 3808–3816.

KRAVCHENKO, A. G., CHOI, H. & MOIN, P. 1993 On the relation of near-wall streamwise vortices to wall skin friction in turbulent boundary layers. *Phys. Fluids* A **5**, 3307–3309.

LEE, C., KIM, J. & CHOI, H. 1998 Suboptimal control of turbulent channel flow for drag reduction. *J. Fluid Mech.* **358**, 245–258.

NAGATA, M. 1990 Three-dimensional finite-amplitude solutions in plane Couette flow: bifurcation from infinity. *J. Fluid Mech.* **217**, 519–527.

PANTON, R. L. 2001 Overview of the self-sustaining mechanisms of wall turbulence. *Prog. Aerosp. Sci.* **37**, 341–383.

PARK, J., HWANG, Y. & COSSU, C. 2011 On the stability of large-scale streaks in turbulent Couette and Poiseuille flows. *C. R. Mécanique* **339**, 1–5.

PUJALS, G., GARCIA-VILLALBA, M., COSSU, C. & DEPARDON, S. 2009 A note on optimal transient growth in turbulent channel flows. *Phys. Fluids* **21**, 015109.

ROBINSON, S. K. 1991 Coherent motions in the turbulent boundary layer. *Annu. Rev. Fluid Mech.* **23**, 601–639.

SCHOPPA, W. & HUSSAIN, F. 2002 Coherent structure generation in near-wall turbulence. *J. Fluid Mech.* **453**, 57–108.

SMITH, C. R. & WALKER, J. D. A. 1995 Turbulent wall-layer vortices. In *Fluid Vortices* (ed. S. Green). pp. 235–290. Kluwer.

SWEARINGEN, J. D. & BLACKWELDER, R. F. 1987 The growth and breakdown of streamwise vortices in the presence of a wall. *J. Fluid Mech.* **182**, 255–290.

WALEFFE, F. 1997 On a self-sustaining process in shear flow. *Phys. Fluids* **9**, 883–900.

WALEFFE, F. 1998 Three-dimensional coherent states in plane shear flows. *Phys. Rev. Lett.* **81**, 4140–4143.

WALEFFE, F. 2001 Exact coherent structures in channel flow. *J. Fluid Mech.* **435**, 93–102.

XU, C., ZHANG, Z., TOONDER, J. M. J. D. & NIEUWSTADT, F. T. M. 1996 Origin of high kurtosis levels in the viscous sublayer: direct numerical simulation and experiment. *Phys. Fluids* **8**, 1938–1944.

ZHOU, J., ADRIAN, R. J., BALACHANDAR, S. & KENDALL, T. M. 1999 Mechanisms for generating coherent packets of hairpin vortices in channel flow. *J. Fluid Mech.* **387**, 353–396.